

# Reactive DC Sputtered $\text{TiO}_2$ Electron Transport Layers for Cadmium-Free $\text{Sb}_2\text{Se}_3$ Solar Cells

Christopher H. Don, Thomas P. Shalvey, Daniya A. Sindi, Bradley Lewis, Jack E. N. Swallow, Leon Bowen, Daniel F. Fernandes, Tomas Kubart, Deepnarayan Biswas, Pardeep K. Thakur, Tien-Lin Lee, and Jonathan D. Major\*

The evolution of  $\text{Sb}_2\text{Se}_3$  heterojunction devices away from CdS electron transport layers (ETL) to wide bandgap metal oxide alternatives is a critical target in the development of this emerging photovoltaic material. Metal oxide ETL/ $\text{Sb}_2\text{Se}_3$  device performance has historically been limited by relatively low fill factors, despite offering clear advantages with regards to photocurrent collection. In this study,  $\text{TiO}_2$  ETLs are fabricated via direct current reactive sputtering and tested in complete  $\text{Sb}_2\text{Se}_3$  devices. A strong correlation between  $\text{TiO}_2$  ETL processing conditions and the  $\text{Sb}_2\text{Se}_3$  solar cell device response under forward bias conditions is observed and optimized. Numerical device models support experimental evidence of a spike-like conduction band offset, which can be mediated, provided a sufficiently high conductivity and low interfacial defect density can be achieved in the  $\text{TiO}_2$  ETL. Ultimately, a  $\text{SnO}_2\text{:F}/\text{TiO}_2/\text{Sb}_2\text{Se}_3/\text{P3HT}/\text{Au}$  device with the reactively sputtered  $\text{TiO}_2$  ETL delivers an 8.12% power conversion efficiency ( $\eta$ ), the highest  $\text{TiO}_2/\text{Sb}_2\text{Se}_3$  device reported to-date. This is achieved by a substantial reduction in series resistance, driven by improved crystallinity of the reactively sputtered anatase- $\text{TiO}_2$  ETL, whilst maintaining almost maximum current collection for this device architecture.

based devices which offer advantages over established silicon solar cells due to the less energy-intensive device fabrication and manufacturing processes. CdTe itself is not without its drawbacks; tellurium scarcity is often cited as a concern for widespread deployment, whilst the toxic heavy metal cadmium inclusion raises questions about end-of-life environmental implications. Thus, it is necessary to explore alternative materials suitable for fulfilling the wide range of evolving PV applications (building integrated (BIPV), tandem top and bottom cell etc.).

Inorganic chalcogenides are another class of materials being studied—many with qualities that make them versatile options for PV. Most notably,  $\text{CuIn}_{1-x}\text{Ga}_x\text{Se}_2$  (CIGS) and kesterite  $\text{Cu}_2\text{ZnSn}(\text{S,Se})_4$  materials (CZTS), have drawn significant scientific interest. Whilst CIGS has achieved an impressive 23.6% power conversion efficiency ( $\eta$ ),<sup>[1]</sup>

the elemental abundance issue remains unsolved with the inclusion of In/Ga, and the requirement for Cd, while reduced, is still present in cadmium sulfide (CdS) as the electron transport layer (ETL). Despite its CdS ETL, CZTS utilizes an entirely

## 1. Introduction

The development of thin-film photovoltaics (PV) has led to the commercialization of polycrystalline cadmium telluride (CdTe)-

C. H. Don, T. P. Shalvey, D. A. Sindi, B. Lewis, J. D. Major  
Stephenson Institute for Renewable Energy  
Department of Physics  
University of Liverpool  
Liverpool L69 7ZF, UK  
E-mail: [jonmajor@liverpool.ac.uk](mailto:jonmajor@liverpool.ac.uk)

D. A. Sindi  
Department of Physics  
College of Science  
Umm Al-Qura University  
Makkah 24382, Saudi Arabia

J. E. N. Swallow  
Department of Materials  
University of Oxford  
Parks Road, Oxford OX1 3PH, UK

L. Bowen  
Department of Physics  
University of Durham  
Durham DH1 3LE, UK  
D. F. Fernandes, T. Kubart  
Department of Electrical Engineering  
Division of Solid-State Electronics  
The Ångström Laboratory  
Uppsala University  
SE-751 03 Uppsala, Sweden

D. Biswas, P. K. Thakur, T.-L. Lee  
Diamond Light Source Ltd, Diamond House  
Harwell Science and Innovation Campus  
Didcot, Oxfordshire OX11 0DE, UK

The ORCID identification number(s) for the author(s) of this article can be found under <https://doi.org/10.1002/aenm.202401077>

© 2024 The Author(s). Advanced Energy Materials published by Wiley-VCH GmbH. This is an open access article under the terms of the [Creative Commons Attribution](#) License, which permits use, distribution and reproduction in any medium, provided the original work is properly cited.

DOI: 10.1002/aenm.202401077

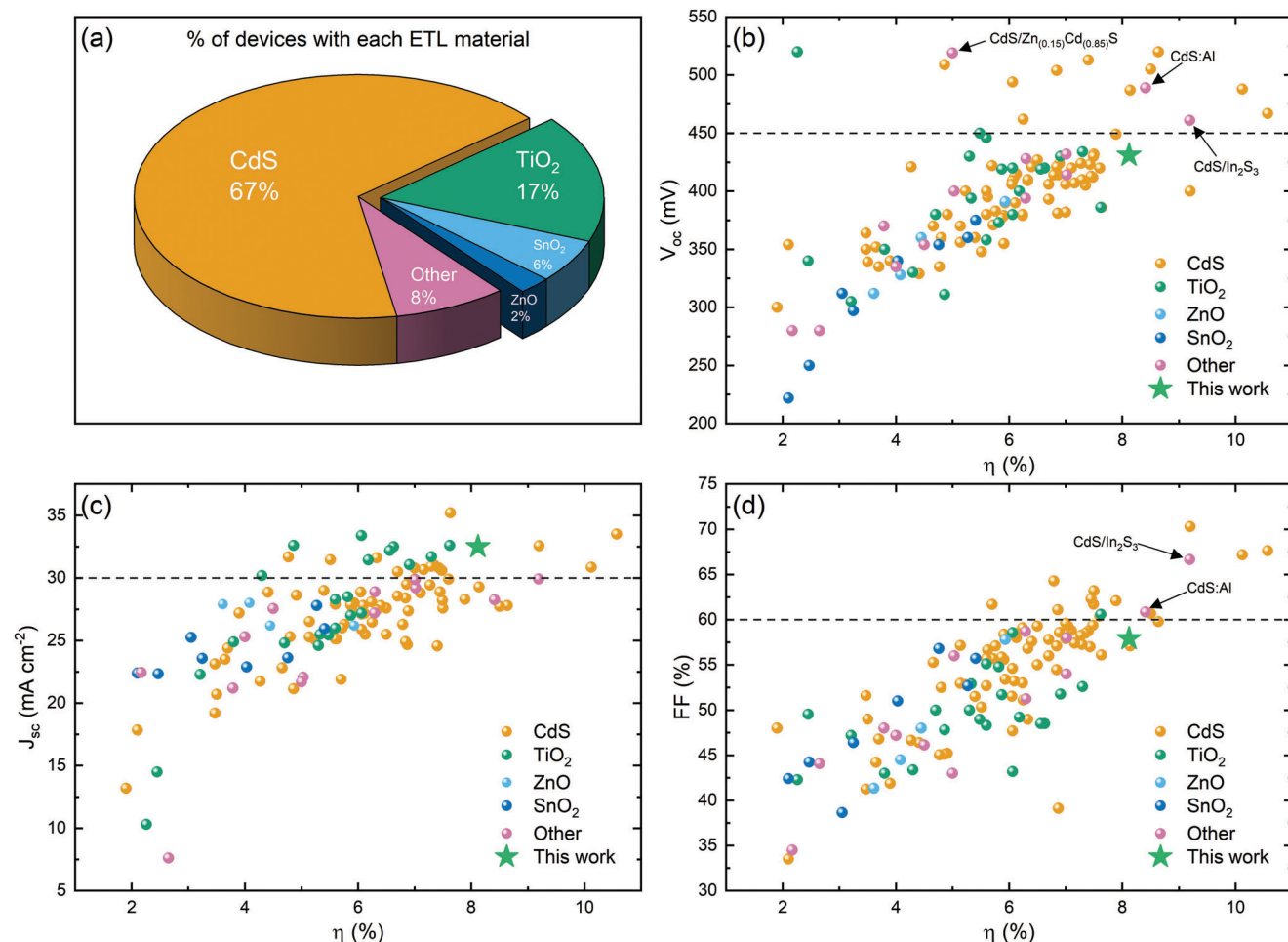


**Figure 1.** a) Percentage of  $Sb_2(S,Se)_3$  devices with each ETL ( $N = 171$ ).  $Sb_2Se_3$  Device performance results for b)  $V_{oc}$ , c)  $J_{sc}$ , and d) FF as a function of  $\eta$  found in the literature for various ETLs. Reproduced and updated with permission.<sup>[13]</sup>

earth-abundant device structure to achieve 13.6%  $\eta$ , however, industrial scalability is in question due to the common formation of unwanted secondary phases during material synthesis.<sup>[2]</sup>

Both antimony selenide ( $Sb_2Se_3$ ) and antimony sulfide ( $Sb_2S_3$ ) are thin-film PV absorber materials currently gathering momentum. With respective optical bandgaps of 1.2 and 1.7 eV,<sup>[3,4]</sup> they offer versatility as both top and bottom cells for tandem devices, but also single-junction capability in the form of the sulfoselenide ( $Sb_2(S,Se)_3$ ) alloy system which allows for bandgap tunability due to the shared 1D “nanoribbon” crystal structure.

In addition to its favorable optoelectronic properties,  $Sb_2(S,Se)_3$  offers earth abundance, low toxicity and high stability.<sup>[5–7]</sup> Rapid increases in device performance have progressed efficiency records to 10.57% and 10.75% for  $Sb_2Se_3$  and  $Sb_2(S,Se)_3$ , respectively.<sup>[8,9]</sup>

A recent life-cycle analysis (LCA) by Resalati et al. has shown that provided efficiencies equivalent to CIGS can be obtained, there would be an environmental benefit of  $Sb_2Se_3$ .<sup>[10]</sup> The study assumed that all devices were in a substrate architecture with a CdS ETL. Thus, eradicating the requirement for Cd completely in the device structure, would offer further advantage to this emerging material. The eventual transition from CdS to metal oxide

ETLs ( $Mg_{1-x}Zn_xO$  and  $SnO_2$ ) during CdTe development was an important step for commercialization.<sup>[11–13]</sup> Undeniably the same must also happen for  $Sb_2(S,Se)_3$ , not only from an LCA standpoint but also in terms of attainable quantum efficiency due to the parasitic absorption of blue light by the 2.4 eV CdS bandgap and resulting transmission loss to the photoactive layer.<sup>[14–16]</sup>

**Figure 1a** distinguishes the ETL of devices reported across  $Sb_2(S,Se)_3$  literature. Pure CdS is evidently the most common, making up two-thirds of devices and often integrated into the more complex structures designated to the “other” category. It is surprising that the combined representation of metal oxides is limited to just 25% of devices, given that the breakthrough  $Sb_2(S,Se)_3$  solar cell work began as an offshoot of dye-sensitized solar cells (DSSC) which incorporated some combination of both planar and mesoporous titanium dioxide ( $TiO_2$ ) at the junction interface.<sup>[17–20]</sup>

Since drawing open-circuit voltage ( $V_{oc}$ ) and short-circuit current density ( $J_{sc}$ ) comparisons for devices across the alloy composition is futile, only  $Sb_2Se_3$  devices from the literature are included in Figure 1b–d ( $N = 135$ ). Looking first at the  $V_{oc}$  of these devices as a function of  $\eta$  (Figure 1b), it can be seen that the only devices consistently exceeding 450 mV are those with a CdS

junction, with the exception of a 520 mV  $\text{TiO}_2$  outlier in an early study by Zhou et al.<sup>[18]</sup> The next highest  $V_{oc}$  reported with  $\text{TiO}_2$  is just below 450 mV, although it would appear that these studies did not include any method to remedy selenium deficiency in the  $\text{Sb}_2\text{Se}_3$  films which is commonly cited as a source of  $V_{oc}$  loss.<sup>[21–25]</sup> It is also worth noting that of the 14 reported devices >450 mV, ten of those were in a substrate device geometry with a Mo hole contact, which may partially explain the relative success of CdS with regards to  $V_{oc}$ .

The performance limiting inter-diffusion at the CdS/ $\text{Sb}_2\text{Se}_3$  interface, observed for devices of both substrate and superstrate geometries, is well-established.<sup>[24,26–28]</sup> In the case of superstrate devices, this introduces constraints on possible high-temperature post-deposition selenization treatments of the absorber which would damage the CdS/ $\text{Sb}_2\text{Se}_3$  interface. The high stability of the  $\text{TiO}_2$ / $\text{Sb}_2\text{Se}_3$  interface during high-temperature exposure is a significant benefit in this regard (Figure S1, Supporting Information).<sup>[29]</sup>

As expected, wide bandgap  $\text{TiO}_2$  ETL  $\text{Sb}_2\text{Se}_3$  devices outperform CdS, in terms of  $J_{sc}$  (Figure 1c), due to the parasitic absorption from the narrow 2.4 eV CdS bandgap heavily studied and optimized in CdTe literature which limits the collection from the blue part of the spectrum. The exception here is a reported 35 mA  $\text{cm}^{-2}$  CdS partner device from Dong et al. which appears to be a record for  $\text{Sb}_2\text{Se}_3$ , although external quantum efficiency (EQE) measurements are absent.<sup>[25]</sup>

Whilst the  $V_{oc}$  advantage in CdS ETL  $\text{Sb}_2\text{Se}_3$  devices over  $\text{TiO}_2$  may be explained by substrate geometry and selenization efforts, the fill factor ( $FF$ ) of the best CdS ETL devices ( $\approx 70\%$ ) is still above that of  $\text{TiO}_2$  ( $\approx 60\%$ ) (Figure 1d). These parameters are of course intrinsically linked through non-radiative recombination, however, low  $\text{Sb}_2\text{Se}_3$  device  $FF$ s cannot be explained purely by  $V_{oc}$ -deficit as illustrated by the 400 mV  $V_{oc}$  device by Li et al. with >70%  $FF$ .<sup>[27]</sup> Clearly, there is still significant room for the development of  $\text{Sb}_2\text{Se}_3$  device architectures to improve selective carrier transport, which appears to be a bigger issue, at present, for metal oxide ETL devices (Figure 1).

The widely implemented organic hole transport layers (HTL) (Spiro-OMeTAD, P3HT etc.) in superstrate devices offer a two-birds-one-stone solution to both low shunt resistance ( $R_{sh}$ ) and forward-bias rollover caused by the  $\text{Sb}_2\text{Se}_3$ /Au interface.<sup>[7]</sup> This is achieved by simultaneously pinhole blocking shunt pathways and improving charge selectivity at the hole contact to improve both average and peak cell  $FF$ s.

For electron transport, there are two studies outside of our group which report on  $\text{TiO}_2$  processing optimization in  $\text{Sb}_2(\text{S},\text{Se})_3$  literature. The first study by Chen et al. varied post-deposition anneal temperatures of their spray-pyrolysis deposited  $\text{TiO}_2$  and concluded that reduced deep-level defects in the 450 °C sample resulted in improved  $\text{Sb}_2\text{Se}_3$  solar cell performance.<sup>[30]</sup> Koltsov et al. compared the effects of vacuum and air annealing of their spray-pyrolysis  $\text{TiO}_2$  and suggested that an initial low-temperature vacuum anneal, prior to the typical 450 °C air anneal, improved performance by reducing organic residues in resulting films.<sup>[31]</sup> Both studies omit current density–voltage ( $J$ – $V$ ) curves for these sections, but a significant  $FF$  dependence is observed in reported  $J$ – $V$  parameters (as low as  $\approx 30\%$  which is approaching a flat line in the power quadrant), suggesting severe “S-shape”  $J$ – $V$  distortion.

Previously, we have reported on  $FF$  limiting  $J$ – $V$  distortion which is induced by charge barriers from defective  $\text{TiO}_2$  ETLs.<sup>[32]</sup> They appear influenced by poor crystallinity, defect-driven photoconductivity and mixed-phase films of this polymorphic material. In the aforementioned study,  $\text{Sb}_2\text{Se}_3$  solar cells with radio frequency (RF) magnetron sputtered  $\text{TiO}_2$  ETLs were deposited from a compound  $\text{TiO}_2$  target, although optimization efforts in this case were limited by reproducibility issues. The stubborn adherence to CdS ETLs, rather than  $\text{TiO}_2$ , may be due to the relative difficulty of producing monophasic  $\text{TiO}_2$  with reliable electronic properties, compared to CdS.

For charge separation and selective carrier transport in solar cells, there must be an asymmetry in the electron and hole conductivities.<sup>[33–35]</sup> In p-i-n heterojunction devices, the functionality of the ETL and HTL is critical to achieve this.<sup>[33]</sup> For efficient selectivity, the ETL/absorber interface is required to have a minimal conduction band offset ( $CBO$ ) and a large valence band offset ( $VBO$ ) to facilitate electron transport whilst impeding hole transport. It is well established that a type-I (“spike”)  $CBO$  can lead to  $J$ – $V$  distortion from the resulting interfacial charge barrier for electrons and a subsequent collapse in device  $FF$ .<sup>[36–40]</sup>

Band position measurements via photoemission spectroscopy for both  $\text{TiO}_2$  and  $\text{Sb}_2\text{Se}_3$  are numerous and hugely variant.<sup>[32,41–45]</sup> Figure S2 (Supporting Information) shows two examples in the literature which report a  $-0.50$  eV  $CBO$  “cliff” and a  $+0.71$  eV  $CBO$  spike (a relative  $CBO$  difference of 1.21 eV).<sup>[42,43]</sup> This variance of band positions for what is an intrinsic material property is of course unphysical and highlights limitations in the band alignment method. Determination of the ionization potential via photoemission introduces measurement uncertainties; spectrometer calibration, charging, linear extrapolation of both the valence band maximum ( $VBM$ ) and secondary electron cutoff ( $SEC$ ), and caveats; surface sensitivity, alignment of Fermi levels, band bending upon interface formation, interface defect pinning. For photoactive materials and multi-layer stacks, there are additional effects from both junction and surface photovoltages which can be induced by stray light, or even the measurement beam itself.<sup>[46]</sup> To obtain the conduction band minima ( $CBM$ ) from the ionization potential, the fundamental energy gap ( $E_g$ ) must be subtracted, the measurement of which is itself non-trivial.<sup>[47]</sup> A study by Shiel et al. compared the  $\text{TiO}_2$ / $\text{Sb}_2\text{Se}_3$   $CBO$  positions obtained with three different band alignment methods and reported  $CBO$  values ranging from a  $+0.11$  eV spike to a  $-0.82$  eV cliff.<sup>[41]</sup>

Given that  $J$ – $V$  distortion from devices with  $\text{TiO}_2$ / $\text{Sb}_2\text{Se}_3$  interfaces appears to be a universal problem,<sup>[30–32]</sup> this may be the best evidence for a  $CBO$  spike of these materials after interface formation. These previous reports, along with the present study, suggest the barrier to electron transport can be mediated by optimized  $\text{TiO}_2$  processing, provided sufficiently high electron conductivities and low interfacial defect densities can be obtained.

In this study, we report a simple, scalable, reproducible method of preparing highly crystalline wide bandgap anatase- $\text{TiO}_2$  thin films for application as the ETL in  $\text{Sb}_2\text{Se}_3$  solar cells. An  $\text{SnO}_2$ :F/ $\text{TiO}_2$ / $\text{Sb}_2\text{Se}_3$ /P3HT/Au device fabricated with a reactively sputtered  $\text{TiO}_2$  ETL achieved an improved 8.12%  $\eta$  due to significantly reduced series resistance ( $R_s$ ) compared to similar device structures. Differences in the  $\text{TiO}_2$  films obtained from both precursor solution and sputtering are compared and

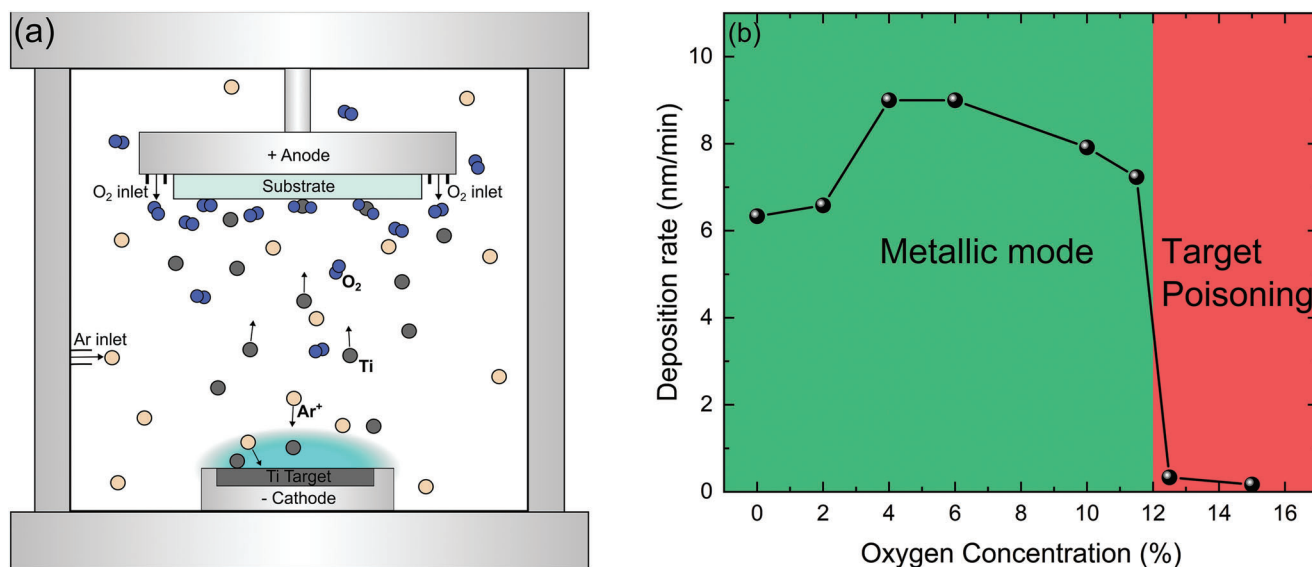


**Figure 2.** a) Illustration of the reactive sputtering process. b) Film deposition rate from a Ti sputtering target as a function of oxygen flow concentration ( $[\text{O}_2/(\text{O}_2 + \text{Ar})] \times 100$ ) at 5 mTorr pressure and  $5 \text{ W cm}^{-2}$  DC power density.

discussed in the context of *FF* variance in completed  $\text{TiO}_2/\text{Sb}_2\text{Se}_3$  devices. The results are supported by numerical simulations which detail the device's physics and serve as a guide to future device processing where additional gains can be made.

## 2. Results and Discussion

### 2.1. Reactive Sputtering of $\text{TiO}_2$ Thin-Films

Magnetron sputter deposition techniques present an opportunity for scalable physical vapor deposition (PVD) of a wide range of materials, irrespective of their melting point. This is of particular importance for materials with low vapor pressure, such as the ETLs explored in  $\text{Sb}_2\text{Se}_3$  heterojunction solar cell device literature ( $\text{CdS}$ ,  $\text{TiO}_2$ ,  $\text{SnO}_2$ ,  $\text{ZnO}$ ). In the case of sputtering from compound ("ceramic") targets of these materials, RF sputtering is frequently needed due to the insulating nature of the sputtering targets. RF sputtering, however, requires more complex hardware and achieves lower deposition rates for the same discharge power as compared to DC sputtering. It is therefore advantageous to use reactive magnetron sputtering from a metallic target by introduction of a reactive gas such as  $\text{O}_2/\text{N}_2$ , in addition to the working gas (Ar), to deliver compound films with a high deposition rate via DC sputtering.<sup>[48,49]</sup>

A major consideration during DC reactive sputtering is that the amount of reactive gas introduced has to be carefully controlled in order to avoid target poisoning. For the case of reactive sputter deposition of titanium oxide films from a Ti target, at high  $\text{O}_2/\text{Ar}$  partial pressures, when the rate of target oxidation from the reactive  $\text{O}_2$  gas exceeds the rate that those species are resputtered back off the surface, then the Ti sputter yield decreases as a result of the surface oxidation.<sup>[50]</sup> This further accelerates the target oxidation, and a runaway effect essentially reduces the deposition rate to a fraction of that achieved at lower  $\text{O}_2/\text{Ar}$  partial pressures. This process exhibits a hysteresis effect whereby the  $\text{O}_2$  flow rate must be significantly reduced below the partial

pressure which induces target poisoning to return it to the metallic state.<sup>[51]</sup> The two regions with very different deposition rates are shown in Figure 2b. Although a high deposition rate can be achieved in the metallic mode, the deposited film is typically oxygen deficient.

The customary approach to preparing anatase- $\text{TiO}_2$  is to initially fabricate an amorphous film at a low temperature ( $<150^\circ\text{C}$ ), and subsequently sinter in air at  $\approx 450^\circ\text{C}$  which recrystallizes the amorphous  $\text{TiO}_2$  toward anatase- $\text{TiO}_2$ .<sup>[52,53]</sup> Thus, initial titanium oxide films were deposited at room temperature (RT). To test the dependence of reactive oxygen incorporation on deposition rate, films were independently sputtered from a Ti target for 60 min at constant  $\text{O}_2/(\text{O}_2 + \text{Ar})$  flow rate, with a 5 min "pre sputter" in 100% Ar between runs to clean the target surface of residual oxygen and reset any hysteresis conditioning. It can clearly be seen from Figure 2 that target poisoning occurs between 11.5% and 12.5%  $\text{O}_2$  flow rate, although the deposition rate starts to significantly reduce already by 10.0%  $\text{O}_2$ .

As-deposited titanium oxide films sputtered in the metallic mode ( $<10.0\%$   $\text{O}_2$ ) suffer from sub-stoichiometry ( $<2:1 \text{ O}:\text{Ti}$ ), indicated by a visible grey darkening of the film and subsequent reduction in spectral transmission. For the case of RT reactively sputtered films, this is easily remedied by a low temperature post-deposition air anneal at  $200^\circ\text{C}$  for 60 min—well below the typical sintering temperatures employed to form anatase phase  $\text{TiO}_2$  (Figure S3, Supporting Information). This is not the case for metallic Ti films (0%  $\text{O}_2$ ) for which the transmission is reduced even for an increased  $550^\circ\text{C}$  post-deposition air anneal (Figure S4, Supporting Information), or for the case where the substrate is heated during sputter deposition, as discussed later.

Whilst the effects of other sputtering parameters can be explored (target power density, deposition pressure), oxygen utilization and subsequent plasma properties will be affected, thus the target poisoning regime in Figure 2b would need to be calibrated for each case. For this study, a high power density ( $5 \text{ W cm}^{-2}$ ) and low pressure (5 mTorr) were fixed to deliver a high



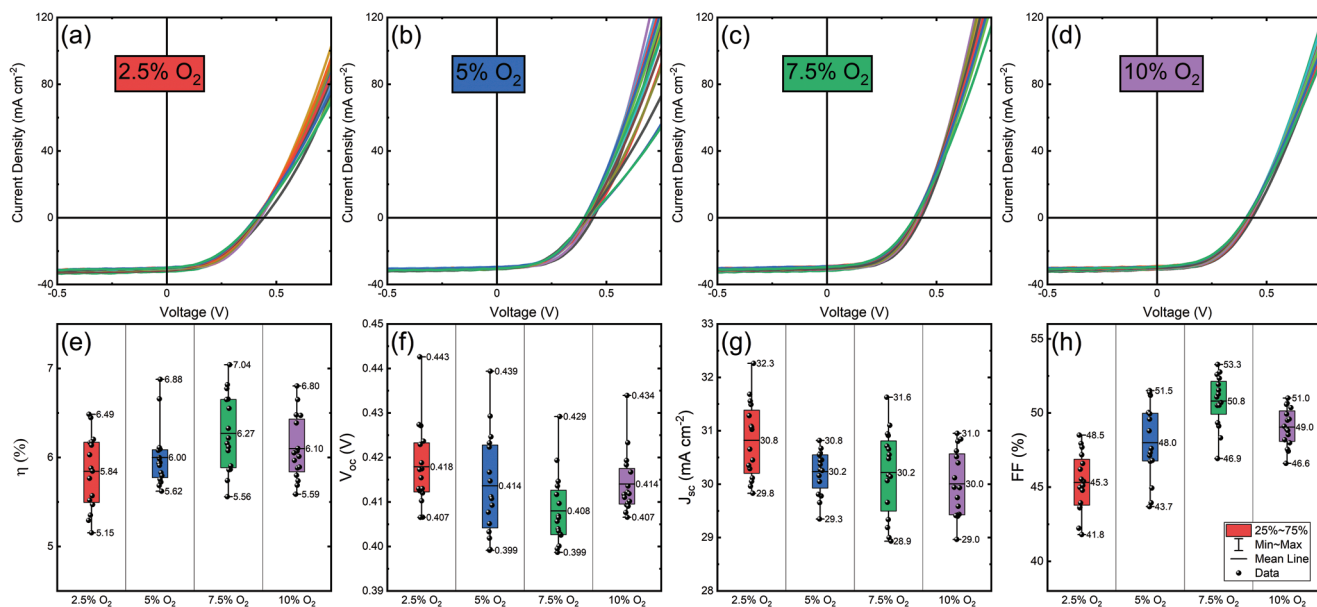


**Figure 3.**  $J$ - $V$  curves at AM1.5 for  $\text{Sb}_2\text{Se}_3$  devices ( $N=16$ ) with reactively sputtered  $\text{TiO}_2$  ETLs sputtered at a) 2.5%, b) 5.0%, c) 7.5%, and d) 10.0%  $\text{O}_2$  flow rate. Box and whisker plots for extracted  $J$ - $V$  parameters e)  $\eta$ , f)  $V_{oc}$ , g)  $J_{sc}$ , and h)  $FF$ .

deposition rate, suitable for industrial scalability. Dedicated  $\text{TiO}_2$  sputtering literature exploring additional parameter space can be found elsewhere.<sup>[49,54,55]</sup>

## 2.2. Device Optimization

After establishing the operating range of reactive  $\text{O}_2$  flow rate during deposition, complete  $\text{Sb}_2\text{Se}_3$  devices were fabricated as outlined in the experimental section with  $\text{TiO}_2$  ETLs of varying  $\text{O}_2$  flow rate (2.5%, 5.0%, 7.5%, and 10.0%) deposited at RT and post-annealed at 450 °C in the air for 60 min. The  $\text{TiO}_2$  film thicknesses for 2.5%, 5.0%, 7.5% and 10.0% were measured as 107, 101, 99, and 70 nm respectively.

The device performance results from **Figure 3** show that the  $\eta$  dependence correlates primarily with  $FF$ . This is driven by improvements in the forward bias regime as seen in **Figure 3a-d** and reduction in  $R_s$  with increasing  $\text{O}_2$  flow rate from 2.5% to 7.5% (**Figure S5**, Supporting Information). Whilst the 10.0%  $\text{O}_2$  devices don't follow the same trend, we attribute that to the thinner  $\text{TiO}_2$  film in this sample which introduces "S-shape"  $J$ - $V$  distortion as will be shown next. As the  $\text{O}_2$  flow rate approaches the target poisoning domain (i.e.,  $\geq 10.0\%$ ), process instability is introduced which limits control of deposition rate and consequent sample reproducibility. Thus, 7.5%  $\text{O}_2$  was selected for further optimization efforts and all subsequent devices presented in this study. However, we consider that operating as close to the target poisoning regime as possible may be beneficial, provided stability is maintained via feedback control systems and plasma emission monitoring.<sup>[56]</sup>

Upon identification of suitable sputtering conditions to provide reproducible  $\text{TiO}_2$  films with high deposition rate and optical transparency, the ETL film thickness was varied to understand the impact on the  $\text{Sb}_2\text{Se}_3$  device performance. The device

$\eta$  results in **Figure 4** again show a strong correlation with  $FF$ , although seemingly through a different mechanism. In this case the introduction of a barrier to charge extraction, indicated by the S-shape  $J$ - $V$  distortion in both the 25 and 60 nm (**Figure 4a,b**)  $\text{TiO}_2$  devices, drastically reduces  $FF$ .<sup>[39,40]</sup> Meanwhile for the device with a 330 nm  $\text{TiO}_2$  ETL, the parasitic resistance contribution to  $R_s$  is increased and current loss is evident in reverse bias, likely due to a reduction in transmission through the thicker window layer. X-ray diffraction (XRD) of the  $\text{Sb}_2\text{Se}_3$  films which produced the devices in **Figure 4** all show a nominal (primarily (211) and (221)) film orientation, free of  $hk0$  flat-lying grains (**Figure S6**, Supporting Information).

In CdTe literature, device  $V_{oc}$  falls considerably when the CdS ETL thickness is reduced below 100 nm.<sup>[11]</sup> Such an effect is not observed here for the case of the  $\text{TiO}_2/\text{Sb}_2\text{Se}_3$  junction where  $V_{oc}$  appears independent of ETL thickness. The study by Kephart et al. concludes that poor band alignment is the cause of  $V_{oc}$  loss. This is further supported by a  $V_{oc}$  improvement after the addition of low electron affinity ( $\chi_e$ ) transport layers which eliminate the cliff-like CBO.<sup>[11]</sup> The distinction between these two opposing behaviors is characteristic of cliff-like and spike-like CBOs for the CdS/CdTe and  $\text{TiO}_2/\text{Sb}_2\text{Se}_3$  interfaces, respectively.

During the transition to metal oxide ETLs, CdTe devices similarly struggled with charge accumulation at the ETL/absorber interface and resulting  $J$ - $V$  distortion,<sup>[11,57-62]</sup> which was eventually alleviated through interface engineering with  $\text{CdSe}_x\text{Te}_{1-x}$  (CST) absorber grading at the junction. The current record  $\text{TiO}_2/\text{Sb}_2(\text{S,Se})_3$  device similarly benefited from absorber grading with a sulfur-rich junction to suppress interfacial carrier recombination.<sup>[63]</sup>

Besides our previous report which details  $J$ - $V$  distortion in devices caused by the  $\text{TiO}_2/\text{Sb}_2\text{Se}_3$  interface,<sup>[32]</sup> to our knowledge, no other such report exists despite indicators in the  $FF$

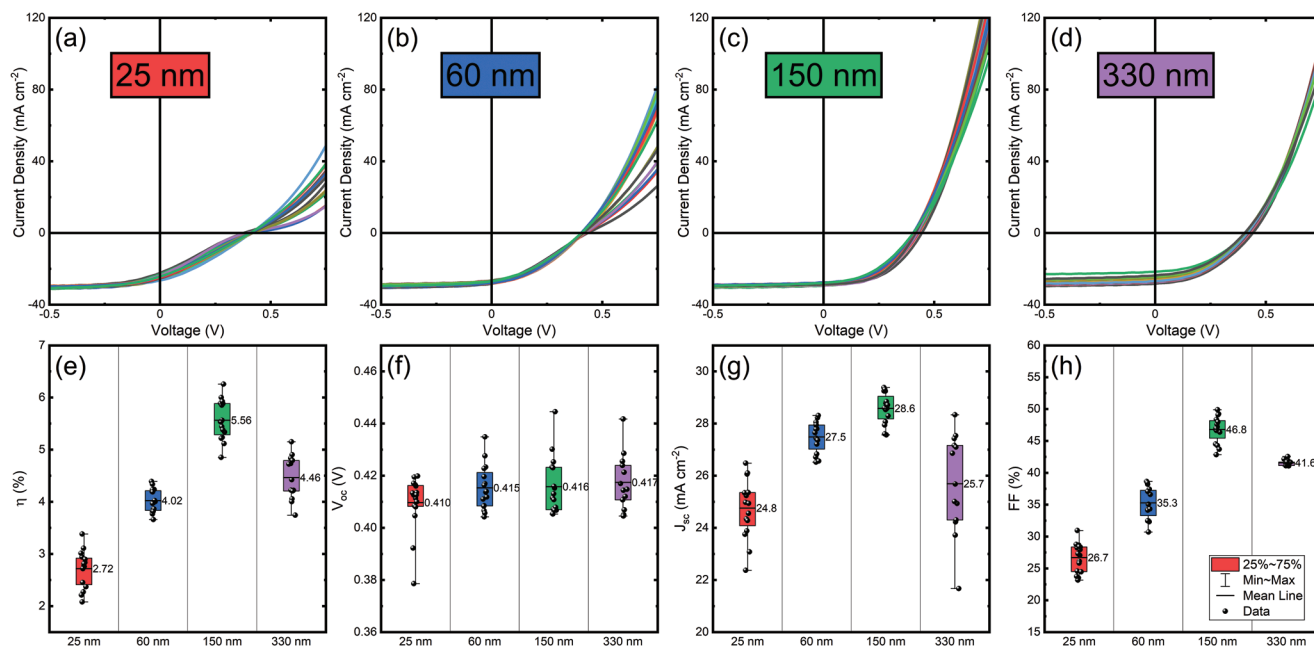


**Figure 4.**  $J$ – $V$  curves at AM1.5 for Sb<sub>2</sub>Se<sub>3</sub> devices ( $N=16$ ) with reactively sputtered TiO<sub>2</sub> ETLs of a) 25 nm, b) 60 nm, c) 150 nm, and d) 330 nm thickness. Box and whisker plots for extracted  $J$ – $V$  parameters e)  $\eta$ , f)  $V_{oc}$ , g)  $J_{sc}$ , and h) FF.

dependencies.<sup>[30,31]</sup> Whether this is due to relatively few groups working on TiO<sub>2</sub> ETL devices or a symptom of groups opting not to report unsuccessful fabrication efforts remains to be seen. Frequent reporting of device  $J$ – $V$  measurements limited to only the “power” quadrant is another factor in obscuring performance-limiting characteristics observable under both reverse and forward bias conditions.

Regardless, for optimization purposes, additional devices were fabricated with a more refined thickness range (100–150 nm) due to the high FF observed for the 99 and 150 nm devices in Figures 3c and 4c. The device results can be found in Figure S7 (Supporting Information), however, no obvious performance trend was observed. Clearly, any marginal gains to be had in this range are currently obscured by larger variances in the full device fabrication process.

### 2.3. TiO<sub>2</sub> Film Characterization

In previous attempts to fabricate TiO<sub>2</sub> ETLs via magnetron sputtering from a compound target, poor crystallinity and lack of phase control in the attained films were a significant issue.<sup>[32]</sup> Those films were similarly sputtered at RT, with a high-temperature post-deposition air anneal, typical of those widely reported in the literature to form polycrystalline anatase phase TiO<sub>2</sub> from chemical precursors. The previous compound sputtered and post-annealed films were amorphous in nature when examined via X-ray diffraction, with a mix of both rutile and anatase signatures identified through bulk Raman and surface X-ray photoemission spectroscopy (XPS) measurements.<sup>[32]</sup> Where strong diffraction is not observed, Raman spectroscopy is a complementary method of characterizing bulk material phase. Due to the nature of the measurement which is sensitive to characteristic

vibrational modes, long-range lattice order is not a prerequisite for phase detection.

To assess the titanium oxide phase attained in films reactively sputtered with 7.5% O<sub>2</sub>, Raman spectra were recorded from RT deposited films with increasing post-deposition air anneal temperatures (Figure 5a). Spectra obtained from solution spin-coated TiO<sub>2</sub> films from titanium isopropoxide (TTIP) precursor with an anneal process in the same range are shown in Figure 5b for reference. The emergence of characteristic vibrational modes for anatase-TiO<sub>2</sub> at 280 °C in the reactively sputtered films is significantly lower temperature than is needed to recrystallize the solution spin-coated amorphous films, which show no anatase signal below 375 °C.<sup>[64,65]</sup> The anatase signal intensity continues to increase with temperature up to 450 °C anneal typically employed in literature, and additionally used to produce the SnO<sub>2</sub>:F/TiO<sub>2</sub>/Sb<sub>2</sub>Se<sub>3</sub>/P3HT/Au devices in Figures 3 and 4.

For superstrate PVD-grown absorber devices, a lower ETL anneal temperature is needless, since the substrate temperature during the close-space sublimation (CSS) process can be as high as 490 °C at present. This result of low-temperature anatase-TiO<sub>2</sub> formation does, however, open up the possibility of incorporation into more temperature-sensitive device architectures such as substrate geometry devices and those with flexible polymer substrates or AZO/ITO transparent front contacts.

Core level (CL) XPS at two different photon energies was employed on the reactively sputtered titanium oxide films with various post-deposition anneal temperatures to expose chemical and compositional information. By operating at both soft (1090 eV) and hard (5925 eV) photon energies, relative surface and more bulk-appropriate effects can be discerned.<sup>[41]</sup>

Figure 6a,b shows XPS and hard X-ray photoelectron spectroscopy (HAXPES) Ti 2p spectra, respectively, of the titanium oxide film with four anneal conditions overlaid. It can be seen

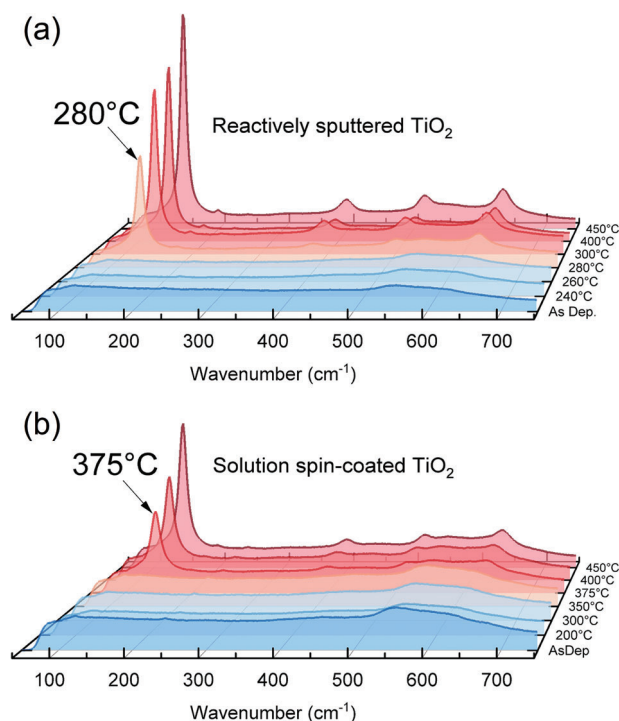


**Figure 5.** Raman spectra of RT a) reactively sputtered and b) solution spin-coated  $\text{TiO}_2$  thin-films deposited on  $\text{SnO}_2\text{:F}$  with various post-deposition air anneal temperatures.

that the titanium is primarily in the assigned 4+ oxidation state associated with  $\text{TiO}_2$ , in agreement with the anatase- $\text{TiO}_2$  Raman signal seen in films annealed at  $>280^\circ\text{C}$  in Figure 5. It can also be seen that most obviously in the as-deposited film but also diminishing with anneal temperature, a low binding energy (BE) shoulder is present. This is widely reported in the literature to belong to  $\text{Ti}^{3+}(\text{Ti}_2\text{O}_3)$ , rather than  $\text{Ti}^{2+}(\text{TiO})$  or metallic Ti which would be expected to feature at much lower BE ( $\sim 3.3$  and  $\sim 4.8$  eV, respectively), relative to  $\text{Ti}^{4+}(\text{TiO}_2)$ .<sup>[66,67]</sup> It should be noted that formal oxidation state assignment here is based purely on those assigned for titanium oxides in XPS literature, however in reality the true chemical bonding mechanisms are more complex.<sup>[68,69]</sup>

By comparing the soft (Figure 6a) and hard X-ray spectra (Figure 6b), it can be seen that the  $\text{Ti}_2\text{O}_3$  feature increases in the as-deposited film for the hard photon energy compared to the soft as we probe deeper into the material. Whilst air exposure was limited to  $\approx 3$  h between film deposition and UHV loading, this suggests some natural oxidation of the surface toward more stoichiometric  $\text{TiO}_2$ , relative to the bulk. This surface and bulk comparison also provide good evidence that although sub-stoichiometric  $\text{TiO}_2$  was deposited via the reactive sputtering method, the post-deposition air anneal treatment is oxidizing subsurface titanium toward 2:1 O/Ti  $\text{TiO}_2$ . According to the phase diagram from Samsonov,<sup>[70]</sup> later reproduced by Diebold,<sup>[71]</sup>  $\text{Ti}_2\text{O}_3$  is the dominant phase for  $1.2 < \text{O/Ti} < 1.6$ , although the oxygen content in as-deposited films reactively sputtered at 7.5%  $\text{O}_2$  is likely much higher than this based on the significant  $\text{Ti}^{4+}(\text{TiO}_2)$  photoemission signal. Extinction of the  $\text{Ti}^{3+}$  HAXPES feature is the best evidence for achieving 2:1 stoichiometry at least beyond the reso-

lution of alternative methods of composition determination such as energy dispersive X-ray spectroscopy (EDX).

Another feature of the spectra is the shift to higher BE of the  $\text{Ti}^{4+} 2p_{3/2}$  CL with increased anneal temperature. Since the CL $\rightarrow$ valence band (VB) energy distance is considered a material constant, this suggests the VB $\rightarrow$ Fermi level ( $E_F$ ) is increasing, i.e., the material is becoming more n-type. Full peak fitted spectra (Figures S8 and S9, Supporting Information), extracted peak positions and widths (Tables S1 and S2, Supporting Information), along with information regarding fitting constraints applied can be found in the supplemental information.

Grazing incidence X-ray diffractograms (GIXRD) in Figure 7 confirm highly crystalline anatase- $\text{TiO}_2$  is formed via the reactive sputtering and post-deposition air anneal method due to the intense, narrow diffraction peaks which agree well with the anatase PDF card (9008216), although shifted to a higher  $2\theta$  angle relative to the simulated powder reference. This effect is due to refraction of the X-ray beam which occurs for incident angles approaching the critical angle.<sup>[76]</sup> The anatase- $\text{TiO}_2$  peak intensity increases considerably in the  $450^\circ\text{C}$  annealed film relative to the  $280^\circ\text{C}$ , indicating some crystallinity improvement in the anatase- $\text{TiO}_2$  between this temperature range. No additional signal from rutile- $\text{TiO}_2$  is observed at  $450^\circ\text{C}$  demonstrating that the annealing treatment is below the threshold for anatase-rutile conversion, in this case, reported to occur between  $400\text{--}1200^\circ\text{C}$  dependent on the crystalline quality of the anatase.<sup>[64]</sup> The peak widths observed here for reactively sputtered- $\text{TiO}_2$  films are far narrower than is attained via fabrication of TTIP solution spin-coated  $\text{TiO}_2$  films with equivalent post-deposition anneal conditions (Figure S10, Supporting Information). An additional peak is observed at  $24.2^\circ$  due to radiation contamination of W filament on the Cu anode. Calculated anatase- $\text{TiO}_2$  spectra from a W  $L\alpha$  source are included in Figure S10 (Supporting Information).

Scanning electron microscopy (SEM) images of the reactively sputtered  $\text{TiO}_2$  films—both as-deposited and post-annealed—show no apparent morphological reconstruction of the large 100 nm agglomerations despite significant changes in Raman, XPS and GIXRD (Figure 8). It is possible that the grainy texture within the agglomerations is softening and becoming more rounded with the post-deposition air anneal treatment. A high-resolution transmission electron microscopy (HRTEM) image of the final  $\text{TiO}_2$  film, taken from a device cross-section, is shown in Figure 8d. Both the electron contact ( $\text{SnO}_2\text{:F}$ ) (red) and absorber ( $\text{Sb}_2\text{Se}_3$ ) (green) interfaces with the  $\text{TiO}_2$  ETL can be observed in the bottom-left and top-right of the image, respectively. The high level of crystallinity achieved via the reactive sputtering method is evident throughout the bulk and also in the near-interface regions. This is not the case for  $\text{TiO}_2$  fabricated via the solution spin-coated method, which shows little diffraction (Figure S11, Supporting Information). No inter-diffusion is observed at the  $\text{TiO}_2/\text{Sb}_2\text{Se}_3$  interface. Crystalline  $\text{Sb}_2\text{Se}_3$  ribbons demonstrate favorable adhesion to the  $\text{TiO}_2$  despite its roughness which results from the conformal sputtered coating of the  $\text{SnO}_2\text{:F}$ .<sup>[32]</sup> This level of ETL material and interface quality is necessary from a device perspective to achieve electron selectivity. The large  $\text{Sb}_2\text{Se}_3$  grain structure obtained via CSS growth on the sputtered  $\text{TiO}_2$  is shown in Figure 8e.

Depositing  $\text{TiO}_2$  films at increased substrate temperature was explored. These films were post-annealed as standard, however,

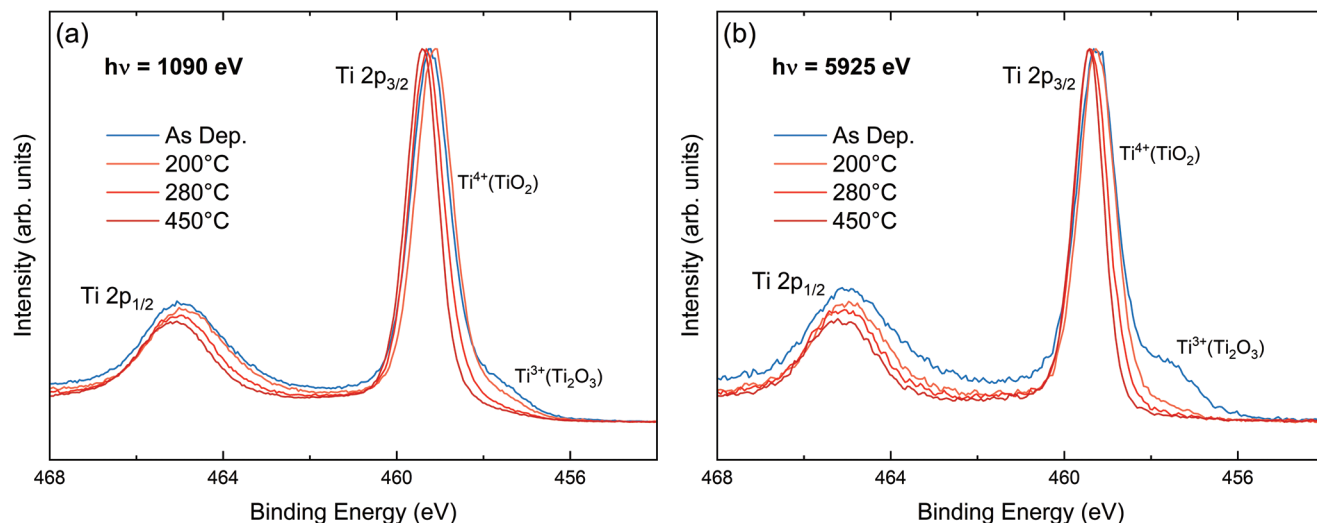


**Figure 6.** a) XPS and b) HAXPES Ti 2p core level photoemission spectra for titanium oxide films as deposited on  $\text{SnO}_2\text{:F}$ , and with 200, 280, and 450 °C post-deposition air anneals. Spectra have been normalized to the  $\text{Ti}^{4+}(\text{TiO}_2)$   $2p_{3/2}$  peak.

it was observed that the post-anneal in this case did not fully remedy the as-deposited oxygen deficiency, as shown by the optical transmission results in Figure S12 (Supporting Information). Raman spectra of these films show anatase at low temperatures, with mixed anatase-rutile phase observed at 200 °C and entirely rutile phase at 300 °C (Figure S13, Supporting Information). Thus, it would appear that the crystallization that occurs as a result of the high substrate temperature during deposition is deleterious in the case of polymorphic  $\text{TiO}_2$  due to the effect of unwanted mixed-phase formation and suboxide  $\text{Ti}_2\text{O}_3$  which is “locked-in” during deposition. Similar unwanted grain formation before the high-temperature anneal in solution spin-coated films may also act to impede final state crystalline quality.

In many cases, ETL characterization is either omitted from studies entirely, or substitute thicker films are deposited on alternative substrates (e.g., Si) to boost the diffraction signal. Another reason for substrate substitution is to simplify optical measurement for bandgap determination via the Tauc method,<sup>[77]</sup> although that presents its own limitations.<sup>[47]</sup> Clearly, this reduces the device relevance as the growth substrate and film thickness play crucial roles in material characteristics. The reasoning often given is that the films are simply too thin for characterization. While this may be true in some cases (resource and measurement dependent), clearly poor crystallinity in the acquired films is another deciding factor.<sup>[32]</sup> This effect of substrate dependant phase formation dynamics is highlighted in Figure S14

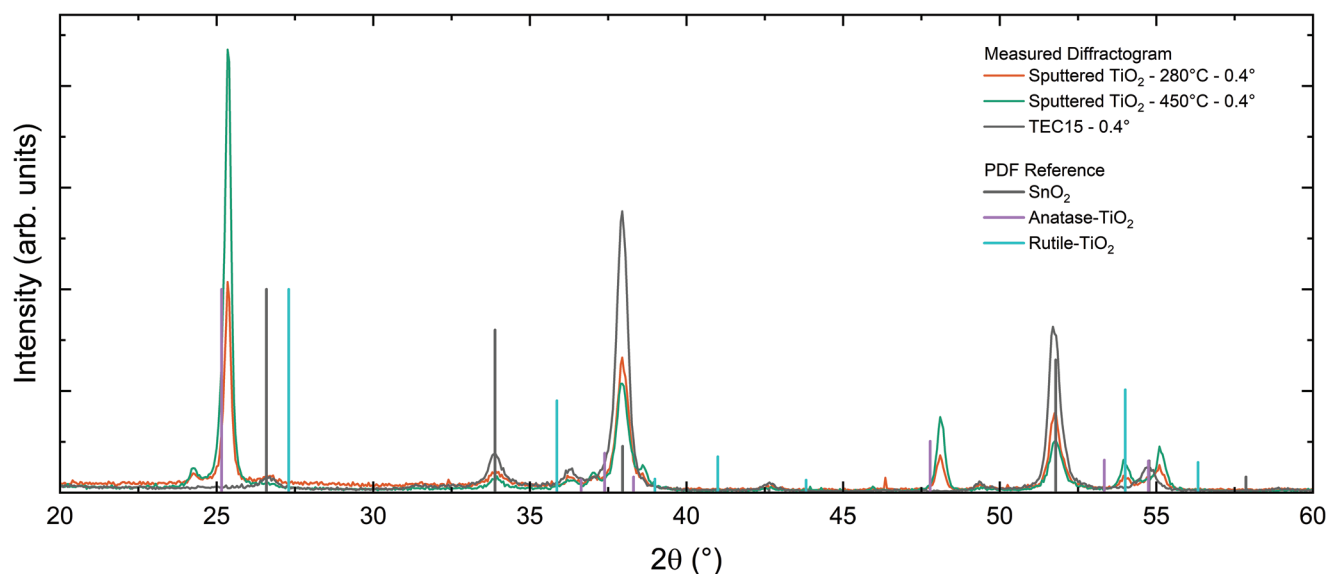


**Figure 7.** GIXRD for reactively sputtered titanium oxide films annealed at 280 and 450 °C, along with a  $\text{SnO}_2\text{:F}$  TEC15 substrate diffractogram for reference. Incident X-ray angle fixed at  $0.4^\circ$ . Also included are powder diffraction file (PDF) cards 9007433, 9008216, and 9004143 for  $\text{SnO}_2$ , anatase- $\text{TiO}_2$ , and rutile- $\text{TiO}_2$ , respectively.<sup>[72–75]</sup>



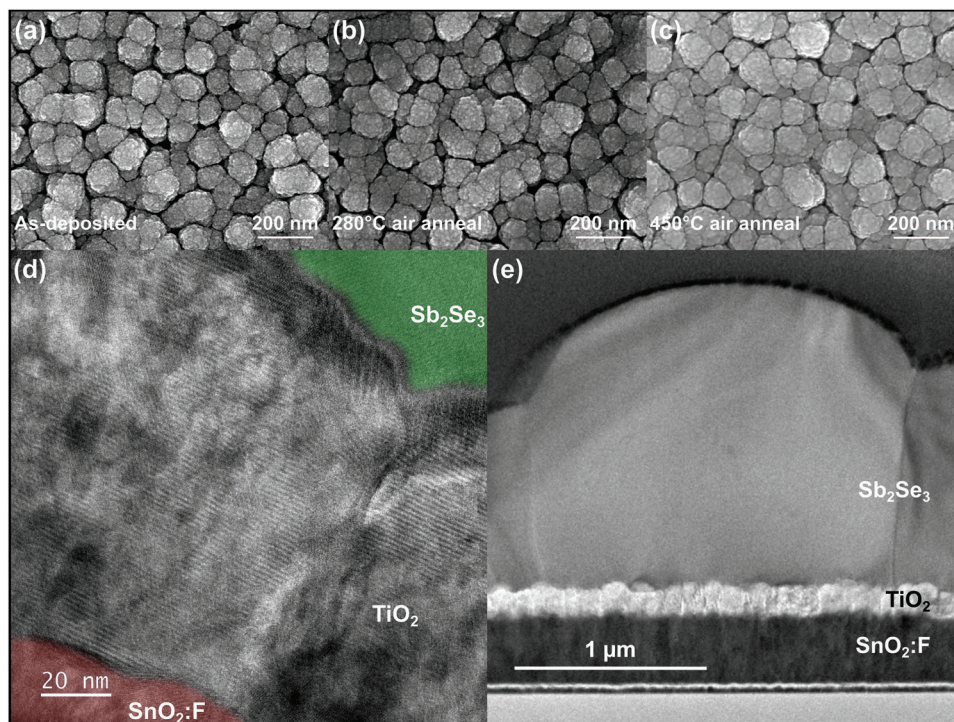


**Figure 8.** SEM of reactively sputtered titanium oxide films a) as-deposited and both b) 280 °C and c) 450 °C post-deposition air annealed. d) HRTEM of  $\text{TiO}_2$  ETL cross-section from the completed device. e) Bright field TEM of  $\text{SnO}_2\text{:F}/\text{TiO}_2/\text{Sb}_2\text{Se}_3$  cross-section.

(Supporting Information), where a witness Si substrate sample shared the same  $\text{TiO}_2$  deposition run as an  $\text{SnO}_2\text{:F}$  substrate, but resulted in anatase and rutile phase  $\text{TiO}_2$  films in the respective cases. Measurement of carrier concentration and mobility via the Hall effect, for example, becomes problematic in this respect, due to the requirement for film deposition onto non-conductive substrates. Interestingly, a  $\text{Sb}_2\text{Se}_3$  device fabricated with the rutile- $\text{TiO}_2$  ETL reached a respectable 6.79%  $\eta$  (Figure S15, Supporting Information), demonstrating that anatase is not the only  $\text{TiO}_2$  polymorph that can function as a high-performance ETL.

## 2.4. Champion $\text{Sb}_2\text{Se}_3$ Device

To properly assess the capability of  $\text{Sb}_2\text{Se}_3$  heterojunction solar cell devices with the highly anatase reactively sputtered  $\text{TiO}_2$  films, additional devices were fabricated with more optimized  $\text{Sb}_2\text{Se}_3$  films. Literature regarding performance of  $\text{Sb}_2\text{Se}_3$  solar cells largely focuses on optimization of the absorber layer itself, with grain structure, nanoribbon orientation, Sb/Se ratio and implementation of interfacial layers all reported as viable methods to achieve this.<sup>[8,27,43,78–84]</sup> In our own experience of growing  $\text{Sb}_2\text{Se}_3$  on  $\text{TiO}_2$ , pinholes, interfacial voiding and formation of  $\text{Sb}_2\text{O}_3$  phases have been the biggest challenges for achieving high-quality absorber material.<sup>[26,32,85]</sup>

Details of  $\text{Sb}_2\text{Se}_3$  CSS growth conditions for initial devices from Figures 3 and 4 can be found in the Experimental Section. Whilst CSS conditions are equivalent within each device series, reactor evolution has meant that optimal conditions can drift over time and thus require periodic reoptimization. Figure 9a,b shows

the champion  $\text{Sb}_2\text{Se}_3$  cell with a 120 nm  $\text{TiO}_2$  ETL reactively sputtered at RT with  $5 \text{ W cm}^{-2}$  power and 7.5%  $\text{O}_2$  flow rate, post-annealed in air at 450 °C for 60 min. The  $\text{Sb}_2\text{Se}_3$  film was grown with a two-step CSS process.<sup>[32,86]</sup> An initial seed layer was deposited with  $T_{\text{source}} = 460$  °C,  $T_{\text{substrate}} = 410$  °C at vacuum for 15 min. The subsequent growth step was carried out at  $T_{\text{source}} = 530$  °C and  $T_{\text{substrate}} = 480$  °C at 10 Torr for 10 min. The sample was then rapidly cooled under an  $\text{N}_2$  atmosphere at 350 Torr. The resulting film again shows no diffraction signal from flat-lying hk0-oriented ribbons (Figure S16, Supporting Information).

The  $J$ - $V$  scan in Figure 9a shows the device's resistance to shunting pathways in reverse bias that results from the pinhole blocking organic P3HT HTL, which is well established.<sup>[86,87]</sup> We have demonstrated through previous work<sup>[32]</sup> and optimization of the  $\text{TiO}_2$  films in this present study (Figures 3 and 4) that device  $R_s$  is strongly dependent on the nature of  $\text{TiO}_2$  ETL. The much reduced  $R_s$  of the cell in Figure 9a of  $2.73 \Omega \text{ cm}^2$  (taken at open-circuit) offers promise that cadmium-free  $\text{Sb}_2\text{Se}_3$  devices can retain high  $FF$ , in addition to the inherent current extraction benefit from a wide bandgap ETL. Some light/dark crossover still persists in forward bias, indicative of either remaining interfacial charge barriers or photoconductivity effects.<sup>[37,88]</sup> Whilst there is no significant transformation of the EQE yield under illumination which was observed previously as a result of sputtered- $\text{TiO}_2$  films,<sup>[32]</sup> there remains a noticeable increase in sub-absorber-bandgap collection in the Urbach tail region  $>1030$  nm (Figure 9b). This is surely related to the large  $V_{oc}$ -deficit in  $\text{Sb}_2\text{Se}_3$  photovoltaics, which must be addressed through absorber defect control and doping approaches, largely not yet explored for this newly developing technology.<sup>[13]</sup>

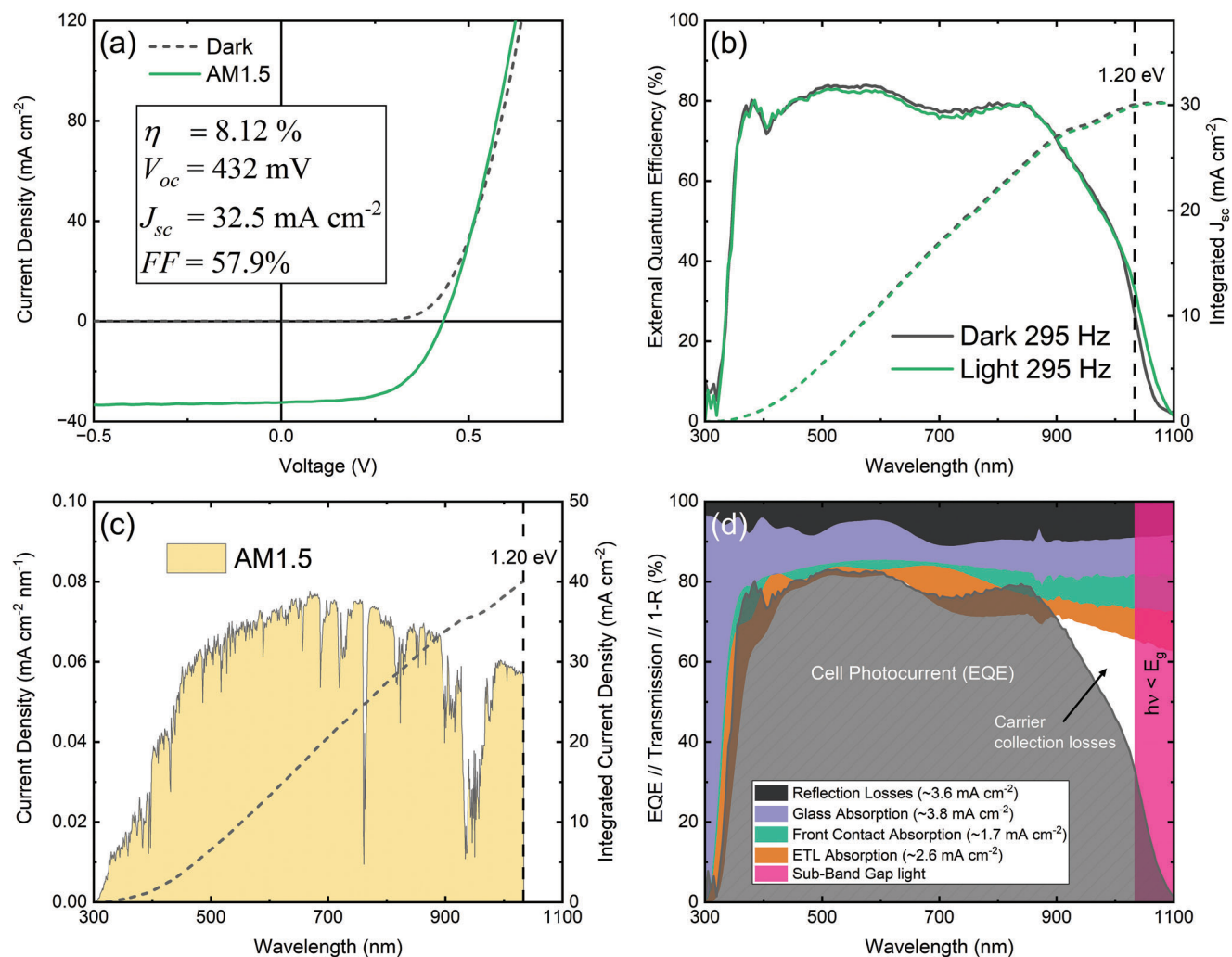


**Figure 9.** a)  $J$ - $V$  and b) EQE of champion  $\text{SnO}_2\text{:F}/\text{TiO}_2/\text{Sb}_2\text{Se}_3/\text{P3HT}/\text{Au}$  cell. c) Maximum attainable current from AM1.5 for an  $\text{Sb}_2\text{Se}_3$  device. d) Quantification of optical losses in a Glass/ $\text{SnO}_2\text{:F}/\text{TiO}_2/\text{Sb}_2\text{Se}_3/\text{P3HT}/\text{Au}$  device.

The  $32.5\text{ mA cm}^{-2} J_{sc}$  (Figure 9a) is approaching the maximum obtainable after accounting for reflection and absorption losses in the 3.2 mm thick soda-lime glass TEC15 substrate (Figure 9c,d). The remaining carrier collection loss is entirely in the infrared region. We anticipate this is primarily due to recombination losses in the  $1.2\text{ }\mu\text{m}$ -thick absorber, which is  $\approx 5\times$  thicker than is employed in the record  $\text{Sb}_2\text{Se}_3$  device.<sup>[8]</sup> Approximate losses for each layer in the stack are provided, although optical interference effects with each subsequent layer results in a discrepancy between the EQE and spectrophotometry without applying the transfer-matrix method.<sup>[89]</sup> The dependence of  $\text{TiO}_2$  thickness on optical interference of the full device stack is highlighted in Figure S17 (Supporting Information).

The significant improvement in the  $FF$  achieved here, compared to our prior work, and the demonstration of such a strong dependence of  $\text{TiO}_2$  ETL film processing on the  $FF$  of subsequent  $\text{Sb}_2\text{Se}_3$  photovoltaic devices, suggests that further optimization of ETLs themselves are effective routes to overcoming current device performance limits. There is, however, still some distance between the  $FF$  of the best  $\text{CdS}/\text{Sb}_2\text{Se}_3$  devices ( $\approx 70\%$ )

and  $\text{TiO}_2/\text{Sb}_2\text{Se}_3$  ( $\approx 60\%$ ). This  $FF$  disparity must be addressed by identifying the source of this sensitivity to interfacial charge accumulation and subsequently correcting charge dynamics at the electron selective contacts.

## 2.5. Device Simulations

The distinction between cliff-like and spike-like CBOs at an ETL/absorber interface was discussed in Section 1. Cliff-like offsets induce  $V_{oc}$ -loss via interfacial recombination and so spike-like offsets are preferred, although for large spikes,  $J$ - $V$  distortion induces  $FF$  loss.<sup>[36–38]</sup> There is a general consensus within PV research that  $\approx 0.4\text{ eV}$  is the limit before which distortion is induced.<sup>[37,39,46,90,91]</sup> This limit is of course system-dependent, with both the ETL and absorber properties defining the electrochemical interface. In the study by Kanevce and Sites et al.<sup>[39]</sup> on the  $\text{CdS}/\text{CIS}$  interface, it was demonstrated that the key value governing this distortion was the difference between the electron quasi-Fermi level and the CBM at the interface. They

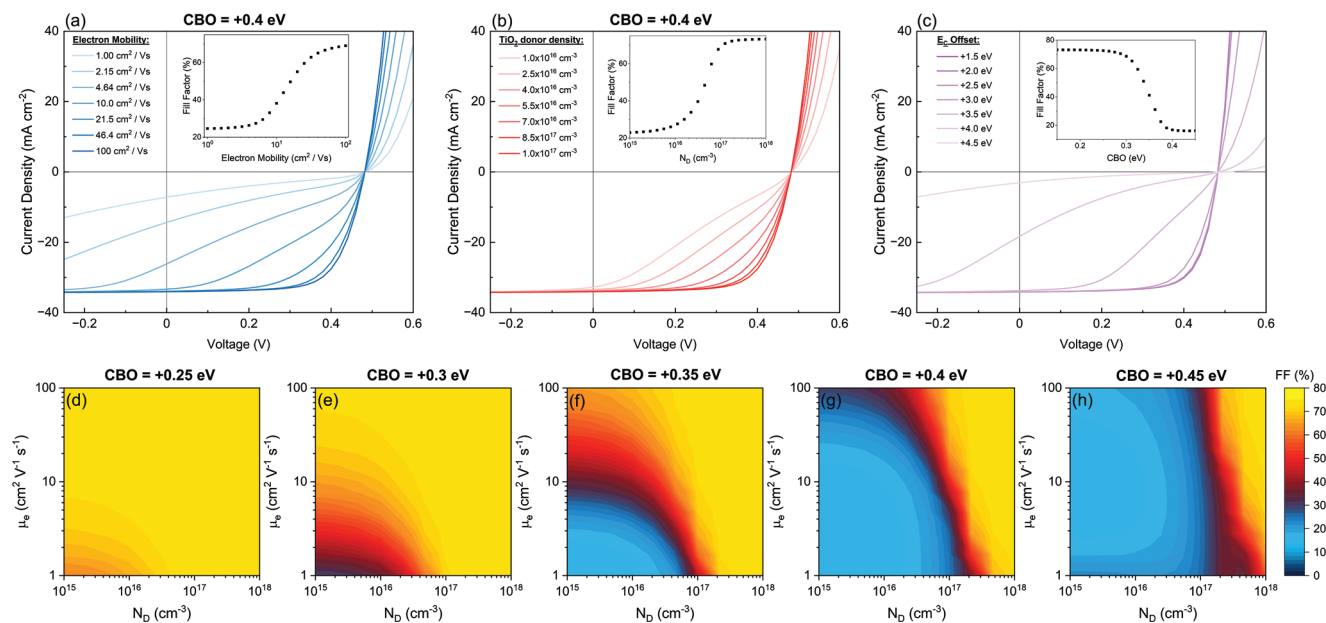


**Figure 10.** SCAPS-1D simulated current density–voltage measurements of  $\text{Sb}_2\text{Se}_3$  devices with  $\text{TiO}_2$  ETLs of varying a) electron mobility ( $\mu_e$ ), b) shallow donor density ( $N_D$ ), c) conduction band offset ( $CBO$ ) with corresponding  $FF$  inset. d–h) Contour plots showing  $FF$  dependency on both the  $\text{TiO}_2$   $\mu_e$  and  $N_D$  for increasing  $CBO$ .

demonstrated that this value is influenced by the bulk  $CBO$ , shallow dopant density ( $N_D$ ), acceptor trap density ( $N_{A_t}$ ) and ETL thickness. Given the variable  $J$ – $V$  distortion observed in the present study, our previous work, and seemingly elsewhere in  $\text{Sb}_2\text{Se}_3$  literature with  $\text{TiO}_2$  ETLs, a model of our device was constructed to allow for interrogation of the underlying device physics. The baseline  $\text{Sb}_2\text{Se}_3$  device model is adapted from Medaille et al.,<sup>[92]</sup> which was defined using experimental data, and is detailed in Tables S4–S6 (Supporting Information).

In the baseline device structure,  $\chi_e$  is set to  $-3.67$  eV for anatase- $\text{TiO}_2$  and  $-4.08$  for  $\text{Sb}_2\text{Se}_3$  ( $CBO = 0.41$  eV), as reported previously.<sup>[32]</sup> Figure 10a,b shows simulated  $J$ – $V$  curves for devices with increasing  $\mu_e$  and  $N_D$  of the  $\text{TiO}_2$ , respectively, at a fixed  $CBO$ . Literature reported values for room temperature  $\mu_e$  of anatase- $\text{TiO}_2$  vary with crystallinity between  $17$   $\text{cm}^2 \text{V}^{-1} \text{s}^{-1}$  for large single-crystals to  $0.1$   $\text{cm}^2 \text{V}^{-1} \text{s}^{-1}$  for  $20$  nm nanoparticles.<sup>[93–96]</sup> As for carrier concentration, values vary between  $10^{16}$  and  $10^{19} \text{cm}^{-3}$ ,<sup>[97]</sup> primarily dependant on bulk  $\text{V}_\text{O}$  formation.<sup>[71]</sup>

In Figure 10a, it is demonstrated that for a fixed  $1 \times 10^{17} \text{cm}^{-3}$   $N_D$ , there is a strong dependence of  $\mu_e$  on the device  $FF$ . Similarly, even with a sufficiently high  $\mu_e$  ( $100 \text{cm}^2 \text{V}^{-1} \text{s}^{-1}$ ),  $J$ – $V$  distortion is induced by lowering  $N_D$  just one order of magnitude (Figure 10b). For completeness,  $J$ – $V$  curves with increasing  $CBO$  for a fixed conductivity are simulated in Figure 10c and show a sharp  $FF$  reduction, as expected, beginning at  $+0.3$  eV  $CBO$  (inset Figure 10c) for the chosen conductivity. The co-dependencies of  $\mu_e$  and  $N_D$  on device  $FF$  are shown in the contour plots of Figure 10d–h for increasing bulk  $CBO$  values. The simulations reveal an abrupt loss in  $FF$  within a small range of reasonable  $\text{TiO}_2$  electronic properties. These results suggest a  $\text{TiO}_2/\text{Sb}_2\text{Se}_3$   $CBO$  spike between  $+0.30$  and  $+0.45$  eV exists, but which experi-

mentally can be mediated by sufficiently high conductivity of the  $\text{TiO}_2$  layer.

In addition to the  $\text{TiO}_2$  bulk electronic properties investigated in Figure 10, the effects of interface states were also explored. Reduction of the  $\text{TiO}_2$  surface is known to produce a mid-gap feature with Ti 3d character in photoemission of both anatase and rutile, which appears  $\approx 2$  eV above the  $V_{BM}$ .<sup>[98,99]</sup> This is observed experimentally in  $\text{TiO}_2$  films fabricated via solution spin-coating and RF sputtered from a compound  $\text{TiO}_2$  target; however this defect peak appears absent in the  $\text{TiO}_2$  films synthesized from the DC reactive sputtering method as shown in Figure S18 (Supporting Information). Hence it seems reasonable to enquire whether this defect state influences the  $J$ – $V$  distortion. The effects of incorporating this acceptor-type interfacial defect  $2.2$  eV above the  $\text{TiO}_2$   $V_{BM}$  are explored in Figure 11.

It is evident that for high interfacial defect densities,  $J$ – $V$  distortion can be induced even for the case where the ETL/absorber  $CBMs$  are nearly aligned ( $CBO = +0.05$  eV), due to Fermi-level pinning, as discussed by Klenk.<sup>[36]</sup> However, in this scenario, a high interfacial defect density increases  $V_{oc}$ , and is more apparent for smaller  $CBO$ s. Presumably, this is linked to the relative energy position of the hole quasi-Fermi level in the  $\text{Sb}_2\text{Se}_3$  to the acceptor-type  $\text{TiO}_2$  surface defect which will decrease as the  $\text{TiO}_2$   $\chi_e$  is decreased in order to investigate the  $CBO$ . Experimentally, this is not observed as  $V_{oc}$  appears largely independent of  $J$ – $V$  distortion (Figure 4).<sup>[32]</sup>

Modulation of charge states in such acceptor-type defects with illumination is further suggested experimentally by photoconductive effects, namely; crossover in the light and dark  $J$ – $V$  curve presented here (Figure 9a),<sup>[37]</sup> and anomalous light-biased EQE measurements exceeding unity, dependant on chopping frequency.<sup>[32]</sup> This is perhaps further evidence of a spike-like



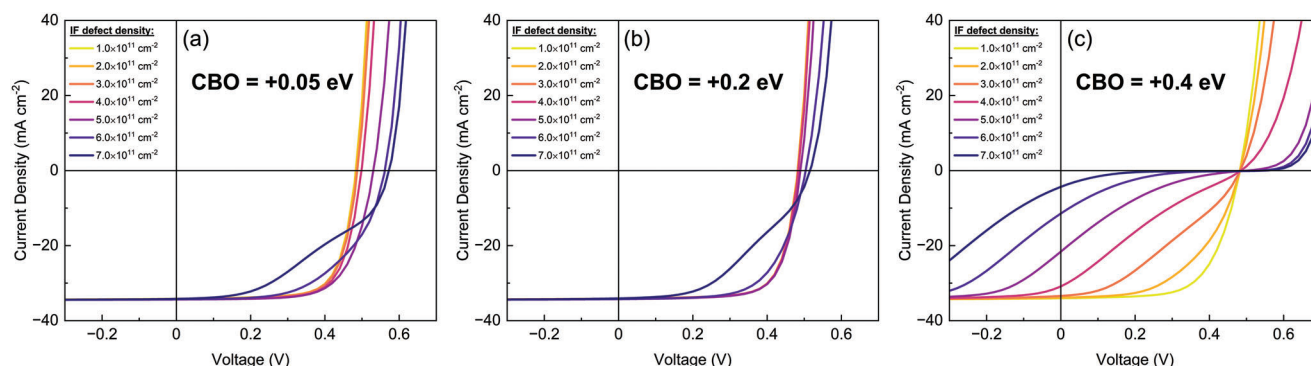


**Figure 11.** SCAPS-1D simulated current density–voltage measurements of  $\text{Sb}_2\text{Se}_3$  devices with  $\text{TiO}_2$  ETLs of varying interfacial defect density for a) +0.05 eV, b) +0.2 eV, and c) +0.4 eV CBO, which is located 2.2 eV above the  $\text{TiO}_2$  VBM.

CBO where the  $V_{oc}$  is invariable and the inflection point of the distortion is fixed at open-circuit, unlike in Figure 11a,b.

Variability in previous work and performance dependence on thickness can be explained by  $\text{TiO}_2$  sensitivity to processing conditions and crystallite size, which are well-established.<sup>[71,93,97]</sup> The device modeling simulations support evidence from select natural band alignment measurements that a spike-like CBO exists between anatase- $\text{TiO}_2$  and  $\text{Sb}_2\text{Se}_3$ ,<sup>[32]</sup> although reported band positions are highly variable as discussed in Section 1. Fundamentally the respective band positions should be largely fixed, and variance in device behavior is more likely regulated by electronic properties. Thus, fabrication of highly crystalline  $\text{TiO}_2$  for enhanced  $\mu_e$  and reduced surface defect density, alongside increased carrier concentration through oxygen-deficient processing, is surely favorable to navigate the CBO of these materials.

The FF of  $\text{TiO}_2/\text{Sb}_2\text{Se}_3$  devices may inherently be limited by such a CBO spike, but  $\text{TiO}_2$  doping approaches are yet to be explored. Alloyed  $\text{Sb}_2(\text{S},\text{Se})_3$  absorbers may offer CBO tunability and Liu et al. have already made progress in this direction, demonstrating an  $R_s$  reduction by increasing the sulfur content (and thus bandgap) in the near-interface region.<sup>[63]</sup> For pure  $\text{Sb}_2\text{Se}_3$  devices, alternative metal oxide ETLs may need to be explored, if the CBO induced by the  $\text{TiO}_2$  interface cannot be alleviated by alternative means.

### 3. Conclusion

In summary, we have investigated the relationship between  $\text{TiO}_2$  thin-film fabrication conditions and the performance of subsequent  $\text{Sb}_2\text{Se}_3$  photovoltaic devices with  $\text{TiO}_2$  acting as an ETL. The method proposed here of reactive DC sputtering from a metallic Ti target offers a high throughput, scalable method of producing high-quality compound  $\text{TiO}_2$  thin films for this photovoltaic application. Through spectrophotometry, SEM, XRD, photoluminescence and Raman spectroscopy characterization, the development of the reactively sputtered  $\text{TiO}_2$  thin-films during the post-deposition anneal process has been studied and compared with conventional spin-coated films from a TTIP precursor solution. Improved crystallinity of anatase- $\text{TiO}_2$  is observed in reactively sputtered films, driving a reduction in  $R_s$  which has historically been a key performance limiting factor for  $\text{Sb}_2\text{Se}_3$  devices of this architecture. This reduction in  $R_s$  and subsequent improve-

ment in FF ultimately delivers the highest efficiency cadmium-free  $\text{Sb}_2\text{Se}_3$  photovoltaic device reported to date.

The effects of varying the  $\mu_e$ ,  $N_D$  and surface acceptor-type defect density of  $\text{TiO}_2$  on device performance are investigated through device modeling simulations which infer the presence of a spike-like CBO between  $\text{Sb}_2\text{Se}_3$  and  $\text{TiO}_2$ . The result provides a robust explanation for FF variability in  $\text{Sb}_2\text{Se}_3$  devices fabricated with  $\text{TiO}_2$  ETLs, and highlights the ETL parameters most critical for developing high-performance cadmium-free devices.

Whilst this step forward only goes some of the way to bridging the gap between state-of-the-art CdS and at-present unconventional wide bandgap metal oxide ETL devices, this result can act as an incentive for an accelerated transition away from CdS ETLs, which surely must happen for the long-term commercialization of  $\text{Sb}_2\text{Se}_3$  solar cells.

### 4. Experimental Section

**Device Fabrication:** All devices fabricated for this study comprised a superstrate-oriented  $\text{SnO}_2:\text{F}/\text{TiO}_2/\text{Sb}_2\text{Se}_3/\text{P3HT}/\text{Au}$  architecture. TEC15 glass (3.2 mm-thick) from Greatcell Solar Materials was used as the soda-lime glass substrate and transparent conductive oxide front contact. The TEC15 substrate was cleaned using isopropyl alcohol, 2% Hellmanex in a deionized water solution and a further 15 min UV ozone treatment. The DC magnetron reactively sputtered  $\text{TiO}_2$  films were sputtered from a 76 mm diameter Ti target (4N purity, PI-KEM) in 5 mTorr pressure at 5 W  $\text{cm}^{-2}$  power density. The combined  $\text{O}_2$ +Ar gas flow rate during sputter deposition was 20 sccm for all films. Oxygen concentration is defined as the percentage of  $\text{O}_2$  flow contributed to total 20 sccm. Spin-coated  $\text{TiO}_2$  films were deposited from a 0.3 M concentration of TTIP in an ethyl alcohol solution. Two 275  $\mu\text{L}$  doses of the solution were sequentially spin-cast at 3000 rpm in a  $\text{N}_2$  atmosphere, with a 10 min 120 °C hot plate anneal after each dose to drive off the remaining solvent. The HiPIMS  $\text{TiO}_2$  films were fabricated by High Power Impulse Magnetron Sputtering in a Lesker CMS-18 deposition system by reactive magnetron sputtering from a Ti target (4N purity) with 100 mm diameter. The HiPIMS process was operated with an average power of 500 W, corresponding to 6.4 W  $\text{cm}^{-2}$ . The pulse on time was set to 100  $\mu\text{s}$  and the frequency to 1 kHz. The depositions were carried out in poisoned (oxide) mode with 60 sccm Ar and 6 sccm  $\text{O}_2$ , at a pressure of 6 mTorr. Unless otherwise stated, as-deposited  $\text{TiO}_2$  films were post-annealed in air at 450 °C for 60 min. Prior to  $\text{Sb}_2\text{Se}_3$  deposition, the  $\text{TiO}_2$  films were ozone-cleaned for 15 min. Alfa Aesar 5N granulate  $\text{Sb}_2\text{Se}_3$  source material was deposited on to the  $\text{TiO}_2$  surface via a two-step CSS process. An initial 15 min seed layer was deposited at a vacuum with respective source and substrate temperatures of 440–450 and 400–410 °C. A subsequent 10 min growth step at 10 Torr  $\text{N}_2$  with respective source



and substrate temperatures of 530 and 480–490 °C followed to deliver a 1.2 µm-thick film. The HTL was deposited from a 10 mg mL<sup>-1</sup> solution of P3HT in chlorobenzene by spin-casting 75 µL at 3000 rpm. 0.1 cm<sup>2</sup> 50 nm thick gold back contacts were then thermally evaporated onto the P3HT surface.

**Material Characterization:** Film thicknesses were measured using a cnc tech AMBIOS XP-200 stylus profilometer. *J*–*V* measurements were taken using a TS Space Systems solar simulator (class AAA) calibrated to AM1.5G. EQE measurements were taken with a Bentham PVE300 system. Quartz-halogen white light-biased EQE was calibrated to a power density of 100 mW cm<sup>-2</sup>. Transmission and reflectivity measurements were taken using a Shimadzu SolidSpec-3700 UV–vis spectrophotometer. Raman spectra were obtained from a Renishaw InVia system operated with a 532 nm laser with 5 s acquisitions at 10 mW for 15 accumulations. The system was calibrated to the 520 cm<sup>-1</sup> peak from a Si wafer, with a resolution of 1 cm<sup>-1</sup>. Photoemission measurements were carried out at the I09 beamline of the Diamond Light Source facility for photon energies of 1090 and 5925 eV. Two-point energy calibration was performed by measuring the Fermi edge and Au 4f<sub>7/2</sub> core-level peak position of a 200 nm Au film at both hard and soft photon energies. A 50 meV step size was used for all core levels with 200 and 70 meV pass energy for hard and soft photon energies, respectively.  $\theta$ – $2\theta$  XRD measurements were obtained from a Rigaku SmartLab diffractometer with a Cu anode ( $\lambda = 1.542$  Å) and a Ge(220) monochromator in parallel beam configuration. Grazing incidence (GIXRD) geometry was used to reduce the intensity from the underlying substrate and selectively probe the TiO<sub>2</sub> layer. This was performed at an incident angle of  $\Omega = 0.4^\circ$  and  $\Omega = 0.6^\circ$ , with a  $5^\circ$  incident slit and  $0.114^\circ$  parallel slit analyzer using non-monochromated Cu K $\alpha_{1,2}$  X-rays. Scanning Electron microscopy was carried out on a Zeiss Sigma 300vp electron microscope operated at 5 keV in Secondary Electron InLens imaging. TEM micrographs were obtained using a JEOL 2100F Transmission Electron Microscope equipped with an Oxford Instrument X-Max 65, operated by 200 keV. The TEM lamella was prepared using an FEI Helios Nano lab 600 MK2.

## Supporting Information

Supporting Information is available from the Wiley Online Library or from the author.

## Acknowledgements

Funding for the work was provided by the EPSRC via EP/T006188/1 and EP/W03445X/1. Diamond Light Source is acknowledged for I09 beam time under proposal SI34642-1. Data files related to the project are available from DOI: 10.5281/zenodo.11220485 or from the corresponding author. The baseline TiO<sub>2</sub>/Sb<sub>2</sub>Se<sub>3</sub> SCAPS-1D device model is available online.

## Conflict of Interest

The authors declare no conflict of interest.

## Data Availability Statement

The data that support the findings of this study are openly available in Reactive DC Sputtered TiO<sub>2</sub> Electron Transport Layers for Cadmium-Free Sb<sub>2</sub>Se<sub>3</sub> Solar Cells at [10.5281/zenodo.11220485](https://doi.org/10.5281/zenodo.11220485), reference number 11220485.

## Keywords

antimony, photovoltaics, Sb<sub>2</sub>Se<sub>3</sub>, selenide, sputtering, solar, TiO<sub>2</sub>

Received: March 8, 2024  
Revised: May 20, 2024  
Published online: June 11, 2024

- [1] M. A. Green, E. D. Dunlop, M. Yoshita, N. Kopidakis, K. Bothe, G. Siefer, X. Hao, *Prog. Photovoltaics* **2023**, *31*, 651.
- [2] G. Fevola, P. S. Jørgensen, M. Verezhak, A. Slyamov, A. Crovetto, Z. I. Balogh, C. Rein, S. Canulescu, J. W. Andreasen, *Phys. Rev. Res.* **2020**, *2*, 013378.
- [3] M. Birkett, W. M. Linhart, J. Stoner, L. J. Phillips, K. Durose, J. Alaria, J. D. Major, R. Kudrawiec, T. D. Veal, *APL Mater.* **2018**, *6*, 084901.
- [4] M. Y. Versavel, J. A. Haber, *Thin Solid Films* **2007**, *515*, 7171.
- [5] X. Wang, R. Tang, C. Wu, C. Zhu, T. Chen, *J. Energy Chem.* **2018**, *27*, 713.
- [6] R. Tang, Z.-H. Zheng, Z.-H. Su, X.-J. Li, Y.-D. Wei, X.-H. Zhang, Y.-Q. Fu, J.-T. Luo, P. Fan, G.-X. Liang, *Nano Energy* **2019**, *64*, 103929.
- [7] N. Fleck, O. S. Hutter, L. J. Phillips, H. Shiel, T. D. C. Hobson, V. R. Dhanak, T. D. Veal, F. Jäckel, K. Durose, J. D. Major, *ACS Appl. Mater. Interfaces* **2020**, *12*, 52595.
- [8] Y. Zhao, S. Wang, C. Li, B. Che, X. Chen, H. Chen, R. Tang, X. Wang, G. Chen, T. Wang, J. Gong, T. Chen, X. Xiao, J. Li, *Energy Environ. Sci.* **2022**, *15*, 5118.
- [9] X. Chen, B. Che, Y. Zhao, S. Wang, H. Li, J. Gong, G. Chen, T. Chen, X. Xiao, J. Li, *Adv. Energy Mater.* **2023**, *13*, 2300391.
- [10] S. Resalati, T. Okoroafor, A. Maalouf, E. Saucedo, M. Placidi, *Appl. Energy* **2022**, *313*, 118888.
- [11] J. Kephart, J. McCamy, Z. Ma, A. Ganjoo, F. Alamgir, W. Sampath, *Sol. Energy Mater. Sol. Cells* **2016**, *157*, 266.
- [12] M. A. Scarpulla, B. McCandless, A. B. Phillips, Y. Yan, M. J. Heben, C. Wolden, G. Xiong, W. K. Metzger, D. Mao, D. Krasikov, I. Sankin, S. Grover, A. Munshi, W. Sampath, J. R. Sites, A. Bothwell, D. Albin, M. O. Reese, A. Romeo, M. Nardone, R. Klie, J. M. Walls, T. Fiducia, A. Abbas, S. M. Hayes, *Sol. Energy Mater. Sol. Cells* **2023**, *255*, 112289.
- [13] C. H. Don, T. P. Shalvey, J. D. Major, *PRX Energy* **2023**, *2*, 041001.
- [14] J. R. Sites, *Sol. Energy Mater. Sol. Cells* **2003**, *75*, 243.
- [15] J. M. Kephart, R. Geisthardt, W. Sampath, in *2012 38th IEEE Photovoltaic Specialists Conference*, IEEE, Austin, TX, USA, **2012**, pp. 000854–000858.
- [16] J. M. Kephart, R. M. Geisthardt, W. S. Sampath, *Prog. Photovoltaics* **2015**, *23*, 1484.
- [17] Y. Itzhaik, O. Niitsoo, M. Page, G. Hodes, *J. Phys. Chem. C* **2009**, *113*, 4254.
- [18] Y. Zhou, M. Leng, Z. Xia, J. Zhong, H. Song, X. Liu, B. Yang, J. Zhang, J. Chen, K. Zhou, J. Han, Y. Cheng, J. Tang, *Adv. Energy Mater.* **2014**, *4*, 1301846.
- [19] Y. C. Choi, T. N. Mandal, W. S. Yang, Y. H. Lee, S. H. Im, J. H. Noh, S. I. Seok, *Angew. Chem., Int. Ed.* **2014**, *53*, 1329.
- [20] Y. C. Choi, D. U. Lee, J. H. Noh, E. K. Kim, S. I. Seok, *Adv. Funct. Mater.* **2014**, *24*, 3587.
- [21] M. Leng, M. Luo, C. Chen, S. Qin, J. Chen, J. Zhong, J. Tang, *Appl. Phys. Lett.* **2014**, *105*, 083905.
- [22] G.-X. Liang, Y.-D. Luo, S. Chen, R. Tang, Z.-H. Zheng, X.-J. Li, X.-S. Liu, Y.-K. Liu, Y.-F. Li, X.-Y. Chen, Z.-H. Su, X.-H. Zhang, H.-L. Ma, P. Fan, *Nano Energy* **2020**, *73*, 104806.
- [23] G. Liang, M. Chen, M. Ishaq, X. Li, R. Tang, Z. Zheng, Z. Su, P. Fan, X. Zhang, S. Chen, *Adv. Sci.* **2022**, *9*, 2105142.
- [24] R. Tang, S. Chen, Z.-H. Zheng, Z.-H. Su, J.-T. Luo, P. Fan, X.-H. Zhang, J. Tang, G.-X. Liang, *Adv. Mater.* **2022**, *34*, 2109078.
- [25] S. Dong, G. Li, J. Hong, R. Qi, S. Yang, P. Yang, L. Sun, F. Yue, *Phys. Chem. Chem. Phys.* **2023**, *25*, 4617.
- [26] L. J. Phillips, C. N. Savory, O. S. Hutter, P. J. Yates, H. Shiel, S. Mariotti, L. Bowen, M. Birkett, K. Durose, D. O. Scanlon, J. D. Major, *IEEE J. Photovoltaics* **2019**, *9*, 544.
- [27] Z. Li, X. Liang, G. Li, H. Liu, H. Zhang, J. Guo, J. Chen, K. Shen, X. San, W. Yu, R. E. Schropp, Y. Mai, *Nat. Commun.* **2019**, *10*, 1.
- [28] R. E. Williams, Q. M. Ramasse, K. P. McKenna, L. J. Phillips, P. J. Yates, O. S. Hutter, K. Durose, J. D. Major, B. G. Mendis, *ACS Appl. Mater. Interfaces* **2020**, *12*, 21730.

- [29] S. Lu, H. Ding, J. Hu, Y. Liu, J. Zhu, R. Kondrotas, C. Chen, J. Tang, *Appl. Phys. Lett.* **2020**, 116, 241602.
- [30] C. Chen, Y. Zhao, S. Lu, K. Li, Y. Li, B. Yang, W. Chen, L. Wang, D. Li, H. Deng, F. Yi, J. Tang, *Adv. Energy Mater.* **2017**, 7, 1700866.
- [31] M. Koltsov, R. Krautmann, A. Katerski, N. Maticiu, M. Krunk, I. Oja Acik, N. Spalatu, *Faraday Discuss.* **2022**, 239, 273.
- [32] C. H. Don, T. P. Shalvey, M. J. Smiles, L. Thomas, L. J. Phillips, T. D. C. Hobson, H. Finch, L. A. H. Jones, J. E. N. Swallow, N. Fleck, C. Markwell, P. K. Thakur, T.-L. Lee, D. Biswas, L. Bowen, B. A. D. Williamson, D. O. Scanlon, V. R. Dhanak, K. Durose, T. D. Veal, J. D. Major, *Adv. Mater. Interfaces* **2023**, 10, 2300238.
- [33] U. Würfel, A. Cuevas, P. Würfel, *IEEE J. Photovoltaics* **2015**, 5, 461.
- [34] U. Rau, T. Kirchartz, *Adv. Mater. Interfaces* **2019**, 6, 1900252.
- [35] A. Onno, C. Chen, P. Koswatta, M. Boccia, Z. C. Holman, *J. Appl. Phys.* **2019**, 126, 183103.
- [36] R. Klenk, *Thin Solid Films* **2001**, 387, 135.
- [37] M. Gloeckler, C. Jenkins, J. R. Sites, *MRS Proc.* **2003**, 763, B5.20.
- [38] M. Gloeckler, J. Sites, *Thin Solid Films* **2005**, 480-481, 241.
- [39] A. Kanevce, M. Gloeckler, A. O. Pudov, J. R. Sites, *MRS Online Proc. Libr.* **2005**, 865, 532.
- [40] R. Saive, *IEEE J. Photovoltaics* **2019**, 9, 1477.
- [41] H. Shiel, O. S. Hutter, L. J. Phillips, J. E. N. Swallow, L. A. H. Jones, T. J. Featherstone, M. J. Smiles, P. K. Thakur, T.-L. Lee, V. R. Dhanak, J. D. Major, T. D. Veal, *ACS Appl. Energy Mater.* **2020**, 3, 11617.
- [42] W. Wang, Z. Cao, H. Wang, J. Luo, Y. Zhang, *J. Mater. Chem. A* **2021**, 9, 26963.
- [43] Y. Wang, R. Tang, L. Huang, C. Qian, W. Lian, C. Zhu, T. Chen, *ACS Appl. Mater. Interfaces* **2022**, 14, 33181.
- [44] W. Wang, L. Yao, J. Dong, L. Wu, Z. Cao, L. Hui, G. Chen, J. Luo, Y. Zhang, *Adv. Mater. Interfaces* **2022**, 9, 2102464.
- [45] J. Han, X. Pu, H. Zhou, Q. Cao, S. Wang, Z. He, B. Gao, T. Li, J. Zhao, X. Li, *ACS Appl. Mater. Interfaces* **2020**, 12, 44297.
- [46] G. Teeter, S. P. Harvey, C. L. Perkins, K. Ramanathan, I. L. Repins, *J. Vac. Sci. Technol. A* **2019**, 37, 031202.
- [47] J. Klein, L. Kampermann, B. Mockenhaupt, M. Behrens, J. Strunk, G. Bacher, *Adv. Funct. Mater.* **2023**, 33, 2304523.
- [48] D. Depla, S. Mahieu, *Reactive Sputter Deposition*, Springer Berlin, Heidelberg **2008**.
- [49] T. Kubart, D. Depla, D. M. Martin, T. Nyberg, S. Berg, *Appl. Phys. Lett.* **2008**, 92, 221501.
- [50] S. Berg, T. Nyberg, *Thin Solid Films* **2005**, 476, 215.
- [51] K. Strijckmans, R. Schelfhout, D. Depla, *J. Appl. Phys.* **2018**, 124, 241101.
- [52] S. Mariotti, O. S. Hutter, L. J. Phillips, P. J. Yates, B. Kundu, K. Durose, *ACS Appl. Mater. Interfaces* **2018**, 10, 3750.
- [53] Y. Hu, L. Huang, B. Che, H. Wang, A. Liu, C. Zhu, R. Tang, T. Chen, *Adv. Funct. Mater.* **2024**, 34, 2314974.
- [54] M. Liao, H. Niu, G. Chen, *Thin Solid Films* **2010**, 518, 7258.
- [55] D. F. Fernandes, L. Österlund, T. Kubart, *Surf. Coat. Technol.* **2023**, 467, 129659.
- [56] T. Kubart, O. Kappertz, T. Nyberg, S. Berg, *Thin Solid Films* **2006**, 515, 421.
- [57] A. Belaidi, R. Bayón, L. Dloczik, K. Ernst, M. Lux-Steiner, R. Könenkamp, *Thin Solid Films* **2003**, 431-432, 488.
- [58] T. Baines, K. Durose, J. D. Major, in *2018 IEEE 7th World Conference on Photovoltaic Energy Conversion (WCPEC) (A Joint Conference of 45th IEEE PVSC, 28th PVSEC & 34th EU PVSEC)*, **2018**, pp. 2974-2979.
- [59] T. Baines, G. Zoppi, L. Bowen, T. P. Shalvey, S. Mariotti, K. Durose, J. D. Major, *Sol. Energy Mater. Sol. Cells* **2018**, 180, 196.
- [60] C. S. Ferekides, D. L. Morel, *Phase I Annual Technical Report October 2005 – September 2006*, **2011**.
- [61] D.-B. Li, Z. Song, R. A. Awni, S. S. Bista, N. Shrestha, C. R. Grice, L. Chen, G. K. Liyanage, M. A. Razooqi, A. B. Phillips, M. J. Heben, R. J. Ellingson, Y. Yan, *ACS Appl. Energy Mater.* **2019**, 2, 2896.
- [62] T. P. Shalvey, H. Bagshaw, J. D. Major, *ACS Appl. Mater. Interfaces* **2022**, 14, 42188.
- [63] C. Liu, S. Wu, Y. Gao, Y. Feng, X. Wang, Y. Xie, J. Zheng, H. Zhu, Z. Li, R. E. Schropp, K. Shen, Y. Mai, *Adv. Funct. Mater.* **2022**, 32, 2209601.
- [64] D. A. H. Hanaor, C. C. Sorrell, *J. Mater. Sci.* **2011**, 46, 855.
- [65] J. Zhang, M. Li, Z. Feng, J. Chen, C. Li, *J. Phys. Chem. B* **2006**, 110, 927.
- [66] R. L. Kurtz, V. E. Henrich, *Surf. Sci. Spectra* **1998**, 5, 179.
- [67] M. C. Biesinger, L. W. Lau, A. R. Gerson, R. S. Smart, *Appl. Surf. Sci.* **2010**, 257, 887.
- [68] D. Koch, S. Manzhos, *J. Phys. Chem. Lett.* **2017**, 8, 1593.
- [69] A. Walsh, A. A. Sokol, J. Buckeridge, D. O. Scanlon, C. R. A. Catlow, *J. Phys. Chem. Lett.* **2017**, 8, 2074.
- [70] G. V. Samsonov, *The Oxide Handbook*, Springer New York, NY, **1982**.
- [71] U. Diebold, *Surf. Sci. Rep.* **2003**, 48, 53.
- [72] W. H. Baur, *Acta Crystallogr.* **1956**, 9, 515.
- [73] M. Horn, C. F. Schwebdtfeger, E. P. Meagher, *Z. Kristallogr. Cryst. Mater.* **1972**, 136, 273.
- [74] E. P. Meagher, G. A. Lager, *Canad. Mineral.* **1979**, 17, 77.
- [75] R. E. Newnham, Y. M. de Haan, *Z. Kristallogr.* **1962**, 117, 235.
- [76] M. Birkholz, P. F. Fewster, C. Genzel, *Thin film analysis by X-ray scattering / Mario Birkholz with contributions by Paul F. Fewster, Christoph Genzel*, Wiley-VCH, Weinheim **2006**.
- [77] J. Tauc, *Mater. Res. Bull.* **1968**, 3, 37.
- [78] Y. Zhou, L. Wang, S. Chen, S. Qin, X. Liu, J. Chen, D.-J. Xue, M. Luo, Y. Cao, Y. Cheng, E. H. Sargent, J. Tang, *Nat. Photonics* **2015**, 9, 409.
- [79] K. Li, C. Chen, S. Lu, C. Wang, S. Wang, Y. Lu, J. Tang, *Adv. Mater.* **2019**, 31, 1903914.
- [80] K. Shen, Y. Zhang, X. Wang, C. Ou, F. Guo, H. Zhu, C. Liu, Y. Gao, R. E. I. Schropp, Z. Li, X. Liu, Y. Mai, *Adv. Sci.* **2020**, 7, 2001013.
- [81] P. Fan, G.-J. Chen, S. Chen, Z.-H. Zheng, M. Azam, N. Ahmad, Z.-H. Su, G.-X. Liang, X.-H. Zhang, Z.-G. Chen, *ACS Appl. Mater. Interfaces* **2021**, 13, 46671.
- [82] Z. Duan, X. Liang, Y. Feng, H. Ma, B. Liang, Y. Wang, S. Luo, S. Wang, R. E. I. Schropp, Y. Mai, Z. Li, *Adv. Mater.* **2022**, 34, 2202969.
- [83] Y. Zhao, S. Wang, C. Jiang, C. Li, P. Xiao, R. Tang, J. Gong, G. Chen, T. Chen, J. Li, X. Xiao, *Adv. Energy Mater.* **2022**, 12, 2103015.
- [84] T. P. Weiss, I. Minguez-Bacho, E. Zuccalá, M. Melchiorre, N. Valle, B. El Adib, T. Yokosawa, E. Spiecker, J. Bachmann, P. J. Dale, S. Siebentritt, *Prog. Photovoltaics* **2023**, 31, 203.
- [85] D. A. Sindi, T. P. Shalvey, J. D. Major, *Mater. Sci. Semicond. Process.* **2024**, 174, 108161.
- [86] O. S. Hutter, L. J. Phillips, K. Durose, J. D. Major, *Sol. Energy Mater. Sol. Cells* **2018**, 188, 177.
- [87] J. Major, L. Phillips, M. A. Turkestani, L. Bowen, T. Whittles, V. Dhanak, K. Durose, *Sol. Energy Mater. Sol. Cells* **2017**, 172, 1.
- [88] R. Scheer, H.-W. Schock, *Chalcogenide Photovoltaics: Physics, Technologies, and Thin Film Devices*, Wiley-VCH, **2011**.
- [89] J. M. Ball, S. D. Stranks, M. T. Hörantner, S. Hüttner, W. Zhang, E. J. W. Crossland, I. Ramirez, M. Riede, M. B. Johnston, R. H. Friend, H. J. Snaith, *Energy Environ. Sci.* **2015**, 8, 602.
- [90] X. Liu, J. R. Sites, *AIP Conf. Proc.* **1996**, 353, 444.
- [91] T. Minemoto, T. Matsui, H. Takakura, Y. Hamakawa, T. Negami, Y. Hashimoto, T. Uenoyama, M. Kitagawa, *Sol. Energy Mater. Sol. Cells* **2001**, 67, 83.
- [92] A. Gon Medaille, K. J. Tiwari, S. Giraldo, M. Placidi, E. Saucedo, Z. Jehl Li-Kao, *Solar RRL* **2022**, 6, 2100911.
- [93] Y. Mi, Y. Weng, *Sci. Rep.* **2015**, 5, 11482.
- [94] T. S. Krasienapibal, T. Fukumura, Y. Hirose, T. Hasegawa, *Jpn. J. Appl. Phys.* **2014**, 53, 090305.
- [95] L. Forro, O. Chauvet, D. Emin, L. Zuppiroli, H. Berger, F. Lévy, *J. Appl. Phys.* **1994**, 75, 633.
- [96] Y. Tamaki, K. Hara, R. Katoh, M. Tachiya, A. Furube, *J. Phys. Chem. C* **2009**, 113, 11741.

- [97] M. C. Sellers, E. G. Seebauer, *Thin Solid Films* **2011**, 519, 2103.
- [98] A. G. Thomas, W. R. Flavell, A. R. Kumarasinghe, A. K. Mallick, D. Tsoutsou, G. C. Smith, R. Stockbauer, S. Patel, M. Grätzel, R. Hengerer, *Phys. Rev. B* **2003**, 67, 035110.
- [99] A. G. Thomas, W. R. Flavell, A. K. Mallick, A. R. Kumarasinghe, D. Tsoutsou, N. Khan, C. Chatwin, S. Rayner, G. C. Smith, R. L. Stockbauer, S. Warren, T. K. Johal, S. Patel, D. Holland, A. Taleb, F. Wiame, *Phys. Rev. B* **2007**, 75, 035105.